Graphene edge chemistry and membrane formation with supramolecular approaches using Pt(II)-terpyridine molecular tweezers

Jiao, A.

Citation

Jiao, A. (2026, June 17). *Graphene edge chemistry and membrane formation with supramolecular approaches using Pt(II)-terpyridine molecular tweezers*. Retrieved from https://hdl.handle.net/1887/4306600

CHAPTER 6

Computational design and self-assembly synthesis of borazine-based free-standing molecular-thin films

Boron-nitride-rich organic thin materials based on borazines have gained significant attention for their potential in nano(opto)electronic and energy storage devices. We address synthetic challenges in producing borazine-based thin films by proposing a dual theoretical and experimental protocol. This combines a multiscale computational approach, using Density Functional Theory and Molecular Dynamics, with synthesis and thin-film formation via the Langmuir-Blodgett technique. The computational design focuses on three key descriptors: π-π stacking interactions, molecular steric hindrance, and dynamic self-assembly orientation. This screening guided the selection of a borazine molecular building block and enabled the successful experimental formation of a borazine film. Solely π-π stacking interactions were found to drive the formation of a bilayer film with a molecular thickness of 2.1 nm, capable of spanning 0.6 µm diameter holes as a free-standing film. The agreement between theory and experiment confirms that the film retains essential features of the borazine molecular crystal, particularly intermolecular offset face-to-face π-π stacking and hexagonal-based pattern orientations. We thus establish a proof of concept for designing and synthesizing borazine-based thin materials, deepen the understanding of molecular interactions in borazine self-assembly, and demonstrate the suitability of the Langmuir-Blodgett technique for fabricating borazine-based 2D materials for energy conversion applications.

This chapter is based on: *Calvani, D.*; Jiao, A.*; Kock T. J. F.; Siegler, M. A.; Sai Sankar Gupta, K. B.; Filippov, D. V.; de Groot, H. J. M.; Sevink, G. J. A.; Schneider, G. F.; Buda, F. Langmuir* ***2026***.

6.1 Introduction

Over the past two decades, developments in borazine and boron-nitride-doped polycyclic aromatic hydrocarbon chemistry have spurred scientific interest in the theoretical design and experimental synthesis of novel hybrid molecular systems based on boron-carbon-nitrogen. The material science applications are diverse,[1,2] including gas-liquid separation, water desalination, sensing techniques, nano(opto)electronics, and energy storage devices.[3,4] The 2005 seminal work by Wakamiya and coworkers laid a cornerstone for research in borazine synthesis and their application in nano(opto)electronics by demonstrating the efficient synthesis of borazine-based aromatic bundle aggregates with a C_3 symmetry and gear-shaped structures.[5] They showed that the π-π stacking interactions between the aromatic moieties guide the aggregation and significantly influence the electronic behavior of the system.[5] Successively, the Bonifazi group has developed, synthesized, and extensively characterized borazine-based molecular systems, yielding various crystal structures with diverse polymorphisms.[6–8] They discussed the role of two-dimensional (2D) molecular-thick borazine-based materials for nano(opto)electronic application,[6–8] and recently also suggested a potential new direction towards borazine-based three-dimensional architectures.[9] Bonifazi and coworkers extensively explored the 2D self-assembly of borazines on metal surfaces, providing a robust approach for studying the fundamental electronic interactions between the molecules and the surface, as well as their impact on borazine orientations. They demonstrated how specific aromatic peripheral groups control the orientation and strength of borazine π-π stacking self-assembly on metal surfaces *via* specific van der Waals and repulsive intermolecular forces.[10,11] While self-assembly on a metal surface enables efficient planarization and interactions between the borazine building blocks, on the other hand, a strong interaction persists between the peripheral aromatic rings and the metal slab.[10,12] This interaction likely results in extremely poor electronic decoupling of the aromatic and flexible carbon backbones from the metal surface,[13] which irreversibly compromises the stability of borazine self-assembled materials during transfer to other substrates and subsequent manipulation. This instability ultimately causes permanent damages that limit the practical application of these materials.[2]

To overcome this key drawback and enable the effective application of borazine-based materials, the development of new rational and systematic approaches is essential. Molecular Langmuir-Blodgett bottom-up self-assembly at the water-to-air interface has shown great promise in producing 2D polycyclic aromatic hydrocarbon-based materials, showing an optimal integration of mechanical stability and chemical reproducibility.[14–16] The selection of molecular building blocks and the careful balance of intermolecular interactions, such as π-π stacking and hydrogen bonding, between these molecular units and the water surface, are crucial for creating tailored 2D self-assembled materials with specific structural characteristics.[14–16] Borazines are attractive candidates for Langmuir-Blodgett self-assembly at the water-to-air interface due to their ability to be functionalized with various sterically hindered aromatic groups, which can be translated into a variety of self-assembly morphologies through chemical versatility and tunability.[5,7,10,11] Additionally, aromatic functionalized borazines exhibit mild reactivity in water, preventing undesired hydrolysis and expanding their application potential,[1,2] which renders borazine Langmuir-Blodgett bottom-up self-assembly a timely research topic.

In this two-step study, we first performed an in-silico screening of π-π stacking motifs that drive self-assembly at the water-to-air interface for Wakamiya-type borazine molecular building block candidates.[5] Second, we synthesized and characterized a borazine-based film with the optimized motif using the Langmuir–Blodgett technique. The computational design focused on Wakamiya-type borazines with a central C_3 symmetric core functionalized with two alternating aromatic moieties (anthracene and phenyl-based groups) at each atom of the central borazine ring. In this work, four borazines, labeled **1**, **2**, **3**, and **4**, were considered; see Figure 6.1A-D. Of these, **2** and **3** have already been synthesized by Wakamiya and coworkers with excellent yields and possessed good stability under standard conditions.[5] Borazine **1** is considered a proper alternative, though it has not yet been synthesized. Borazine **4** is less sterically hindered, and was included in this work for comparison in the rational design strategy, also because its synthesis would likely be affected by hydrolysis. We employed Density Functional Theory (DFT)-based methods in the first step to study the stacking interaction behavior and energetics of the borazines in a dimer configuration. All-Atom Molecular Dynamics (MD) simulations were extensively employed to investigate interactions, orientations, and structure formation by self-assembly at the water-to-air interface under standard and Langmuir-Blodgett conditions. Descriptors such as π-π stacking energetics and molecular orientation were used to select the most promising borazine candidate for synthesis and subsequent characterization, namely B,B′,B″-Tri(9-anthryl)-N,N′,N″-tris(p-isopropyl-phenyl) borazine (borazine **2**, Figure 6.1B). A molecular-thick borazine **2**-based film was experimentally produced *via* the Langmuir-Blodgett technique, transferred onto a silicon wafer or other relevant substrate, and characterized using atomic force microscopy (AFM), scanning electron microscopy (SEM), and fluorescence spectroscopy. This borazine **2**-based film demonstrated free-standing mechanical stability, with structural-mechanical properties, such as molecular thickness, strongly correlated with the theoretical predictions.

This work represents a successful example of experimental synthesis of a π-π stacking driven, bottom-up self-assembly of borazines *via* the Langmuir-Blodgett technique following in-silico rationalization and design, yielding a stable, free-standing, boron-nitride-rich, molecularly-thick organic film. The ultimate goal of this research is to establish an efficient, chemically precise method for the production and tuning of boron-nitride-rich carbon-based nanomaterials, with concrete applications ranging from nano(opto)electronics to energy, CO_2 storage devices, and separation membranes, all contributing to a successful transition to sustainable energy.[1,2]

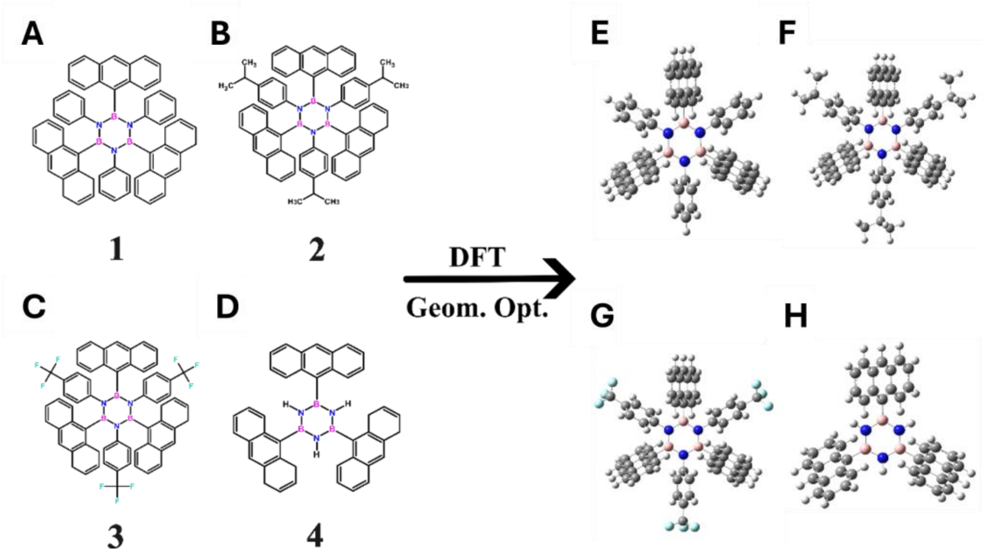

Figure 6.1 Molecular and sketch structures of each borazine considered in the rational design of this work. (A), (B), (C), and (D) represent the molecular structure of borazine **1**, **2**, **3**, and **4**, respectively. (E), (F), (G), and (H) represent, in ball and stick, the corresponding DFT-optimized geometry of the monomer, with hydrogen in white, boron in pink, carbon in grey, nitrogen in blue, and fluorine in cyan, respectively.

6.2 Results and Discussion

6.2.1 DFT Computational Design

For each of the four borazines considered (see Figure 6.1), initial DFT geometry optimization was performed at the level of monomers and respective dimers to estimate the π-π stacking interaction energies that could guide molecular self-assembly (see Computational Methods for the details). The optimized geometries of the dimers reveal their preferred type of π-π stacking interaction for each borazine pair, along with their respective Kohn-Sham (KS) HOMO distributions, as depicted in Figure 6.2. The KS HOMOs of the monomers are shown in the Supporting information Figure S6.1. The anthracene-anthracene interaction is known to be stronger than the benzene-benzene interaction when normalized by the number of carbon atoms.[17] Therefore, only the anthracene-anthracene interaction was taken into account for the estimation of the π-π stacking interaction energy. Borazines **1** and **2** exhibit an offset face-to-face (OFF) or parallel-displaced π-π stacking,[18] with average minimum C-C distances ($D_{min}(C_{anth}-C_{anth})$) between the two anthracene groups of approximately 3.41 Å and 3.34 Å, respectively (see Figure 6.2A-B, and Table 6.1), as schematically represented in Figure 6.2E. On the other hand, the distances between the centers of the aromatic rings in one anthracene moiety and the closest centers of the aromatic rings in the other anthracene moiety ($D_{center}(C_{anth}-C_{anth})$) were approximately 3.95 Å and 3.80 Å, respectively (see Figure 6.2A-B, and Table 6.1), as schematically represented in Figure 6.2E. Interestingly, borazine **2** displayed a slightly firmer localization of the HOMO between the p-isopropyl-phenyl groups and the adjacent interacting anthracenes compared to borazine **1**. This effect can be attributed to the electron-donating effect of the p-isopropyl groups on the phenyl center, which increases the π electron cloud interacting with adjacent anthracenes, and reduces the C-C minimum distance between the interacting anthracene moieties by a dual π-π interacting and repulsive steric effect.[5] This effect results in a stronger π-π stacking energy estimate for borazine **2** than borazine **1**, which were −0.71 kcal mol^{-1} and −0.46 kcal mol^{-1}, respectively (Table 6.1). For the borazine **3** dimer, the withdrawing effect of the trifluoromethyl group ($-CF_3$) present in the *para* position on each phenyl group, along with F-F and F-π interactions, drives the π-π stacking between anthracenes, preferably adopting an edge-to-face (EF) or T-shaped configuration,[18] with an average minimum distance between the two anthracene groups of $D_{min} \approx 3.67$ Å ($D_{center} \approx 4.55$ Å) (see Figure 6.2C and Table 6.1).[19–21] The π-π stacking energy estimate for borazine **3** amounts to −0.60 kcal mol^{-1} (Table 6.1), which is still lower than the value for borazine **2**. Borazine **4** adopted a configuration that optimized π-π stacking between the anthracenes with an average minimum distance of $D_{min} \approx 3.56$ Å ($D_{center} \approx 4.86$ Å) (see Figure 6.2D and Table 6.1). In this case, we noticed increased intercalation of the monomers, resulting from a reduced steric hindrance due to the absence of the phenyl moieties, and an enhanced rotation of the anthracene group relative to the borazine center along one of their equivalent carbon-carbon-boron-nitrogen (C-C-B-N) dihedrals compared to the borazines **1**, **2**, and **3** (see Supporting information Figure S6.2 inset). Steric hindrance between the anthracene moieties in borazines **1**, **2**, and **3** plays a significant role in providing molecular rigidity and in orienting the π-π stacking in OFF and EF configurations within the dimer.[5,10] To analyze the energetics of this torsional degree of freedom, DFT scan calculations along a specific C-C-B-N dihedral were performed for each of the four borazine systems (see Supporting information Figure S6.2 inset). The variation of torsional energy of one representative C-C-B-N dihedral angle over the range of 0−180° is depicted in Figure S6.2. Borazines **1**, **2**, and **3** feature a maximum of around 60 kcal mol^{-1} at approximately 140° when the anthracene is nearly flat relative to the borazine center. In contrast, borazine **4** exhibits a lower energy barrier of approximately 20 kcal mol^{-1} at 120° for the C-C-B-N torsion, as it lacks the three bulky phenyl-based groups connected to the borazine's nitrogen atoms of borazines **1**, **2**, and **3**. This analysis provides insight into the variation in flexibility along the C-C-B-N dihedral angle for each borazine dimer. For the borazine **4** dimer, the higher flexibility and lower steric hindrance, compared to the other borazines, lead to a pronounced intercalated interaction between monomers. The π-π stacking energy estimate of −0.81 kcal mol^{-1} is slightly higher than that of borazine **2** (Table 6.1). This flexibility, the lower steric hindrance, and the π-π stacking energetics could promote disoriented π-π stacking interactions in larger poly-borazines systems. The DFT calculations provide a first clear rationale for selecting borazines based on dimeric packing and flexibility. However, to accurately explore and predict the borazine self-assembly orientation at the water-to-air interface on a nanometer structural level, All-Atom MD simulations are required.

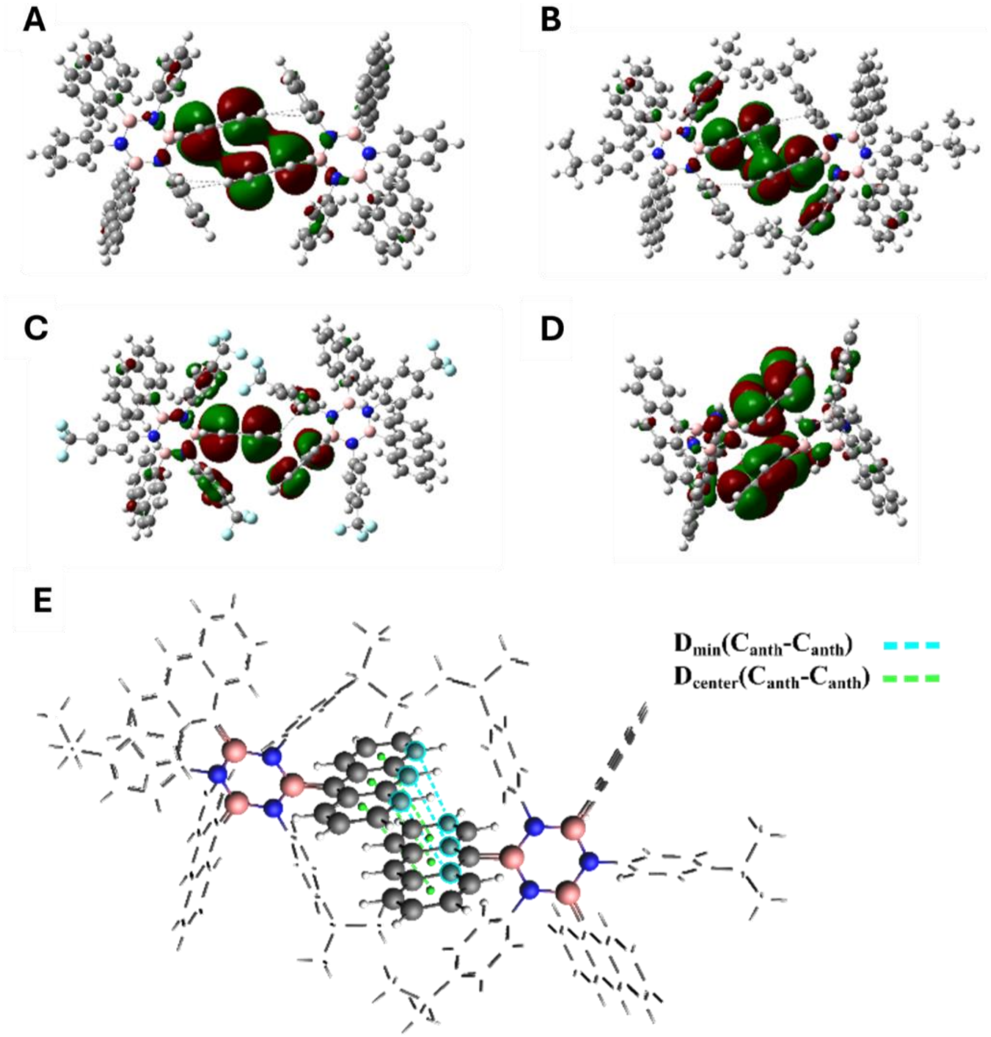

Figure 6.2 DFT-optimized geometry of the dimer configurations and pictorial representations of the KS HOMO for each type of borazine. (A), (B), (C), and (D) represent borazine, **1**, **2**, **3**, and **4**, respectively, with isosurface value = 0.01. (E) A schematic representation of the borazine **2** dimer illustrates the minimum carbon-carbon distance between two adjacent anthracene (anth) of two different monomers reported as $D_{min}(C_{anth}\text{-}C_{anth})$ with dashed cyan lines; the center carbon-carbon distance calculated as the distance between the center of each aromatic ring belonging to one anthracene moiety to the closest center of the aromatic rings of the other anthracene moiety is reported as $D_{center}(C_{anth}\text{-}C_{anth})$ with dashed green lines. In ball and stick, the molecular structures are shown, with hydrogens in white, boron in pink, carbon in grey, nitrogen in blue, and fluorine in cyan. Values of the π-π stacking interaction energy estimates, $D_{min}(C_{anth}\text{-}C_{anth})$, and $D_{center}(C_{anth}\text{-}C_{anth})$ are listed in Table 6.1.

Table 6.1 The π-π stacking interaction energy estimates (kcal mol^{-1}), values of $D_{min}(C_{anth}\text{-}C_{anth})$ (Å), and values of $D_{center}(C_{anth}\text{-}C_{anth})$ (Å) for the DFT-optimized geometry of the dimer configurations for each type of borazine.

Borazine	π-π stacking energy (kcal mol^{-1}) [a]	$D_{min}(C_{anth}\text{-}C_{anth})$ (Å)	$D_{center}(C_{anth}\text{-}C_{anth})$ (Å)
1	-0.46	3.41	3.95
2	-0.71	3.34	3.80
3	-0.60	3.67	4.55
4	-0.81	3.56	4.86

[a] Values were calculated as $\Delta E/N = (E_{\text{dimer}} - 2 \cdot E_{\text{monomer}})/N$, where N is the number of carbon atoms of the 3 anthracene groups in the monomer, equivalent to 42 carbon atoms, for each of the four borazines, respectively.[17]

6.2.2 All-Atom MD computational design

We performed All-Atom MD simulations to study the supra-molecular organization of borazines at the water-to-air interface and room temperature. A water slab was modeled to include two independent water-air interfaces, and various quantities of each borazine (1, 2, 6, or 12 molecules) were considered at the water-air interface (see Computational Methods for details). For borazines **1**, **2**, and **3**, MD results indicated that the molecules were arranged at the water-air interface with the central borazine core essentially parallel to the water surface and with the aromatic edge moieties perpendicular to the water surface (Figure 6.3A-C). In contrast, the self-assembly of borazines **4** gave rise to gross disorder (Figure 6.3D). Analysis of the tilt angle (*Φ*) indicate that as the number of **1**, **2**, or **3** molecules increase, the central borazine ring adopts an increasingly parallel configuration with respect to the water surface, and with tilt angle distributions in the range of 5°< *Φ* < 20° (Figure 6.3E-G). Augmenting the number of borazines from 1 to 12 enhances the contribution of the π-π stacking interactions, which cooperatively dominate over thermally induced disorder, resulting in a hexagonal-based pattern at the water-to-air interface (Figure 6.3A-C).[14,17] This honeycomb-like orientation of borazines **1**, **2**, and **3** is governed by characteristic offset face-to-face (OFF) and edge-to-face (EF) π-π stacking interactions between the aromatic groups as well as the C_3 space group symmetry, producing a hexagonal gear-shaped motif in line with the seminal findings of Wakamiya and coworkers.[5] The distribution of the tilt angle (*Φ*) between the borazine plane and the water surface was investigated after equilibration for 10 ns at 300 K (Figure 6.3E-H). While the distribution of the tilt angle (*Φ*) for borazine **2** is consistently centered around 10° for varying numbers of molecules, a slight shift to

20° is observed for borazine **1** and **3**. In the case of borazine **1**, this shift can be related to the weaker π-π stacking interaction compared to borazine **2** and **3**, according to the DFT results. For borazine **3**, on the other hand, this shift can be explained by the temporary formation of hydrogen bonds between the fluorine atoms in the trifluoromethyl groups and the oxygens of the water molecules at the surface. Hydrogen bonding can compete with the π-π stacking interactions and tends to reorient the borazines **3**.[14] For borazines **1**, **2**, and **3**, we observed that the OFF and EF π-π stacking interactions lead to either clockwise or anticlockwise orientations (Figure 6.3A-C), comparable to those reported by Bonifazi and coworkers for similar borazines on metal surfaces.[10] Nevertheless, in our case, the interactions between the non-amphiphilic borazines **1**, **2**, and **3** and the water slab are primarily repulsive, resulting in a weakly defined chirality of the arrangement, clockwise or anticlockwise. Moreover, this repulsion would likely result in a structure that is more decoupled from the water surface when compared to the one observed on metal surfaces.[10] For borazine **4**, the lack of aromatic substituents on the borazine's nitrogen atoms leads to weak steric hindrance. This allows for energetically stable intercalated but disoriented self-assembly configurations at the water-to-air interface (Figure 6.3D), characterized by a broad tilt angle distribution ranging from 10° to 90°, in stark contrast to borazines **1**, **2**, and **3** (Figure 6.3H). The self-assembly disorder observed for borazine **4** is also attributed to a more favorable rotation of the anthracene moieties compared to the other borazines, detected in the DFT analysis of the C-C-B-N torsion. Accordingly, based on the most energetically favorable π-π stacking interactions (Table 6.1), the optimal orientation at the water-to-air interface at room temperature (Figure 6.3F), and the good synthetic yield previously reported by Wakamiya and coworkers,[4] borazine **2** was selected for synthesis and consequent bottom-up film self-assembly *via* the Langmuir-Blodgett technique.

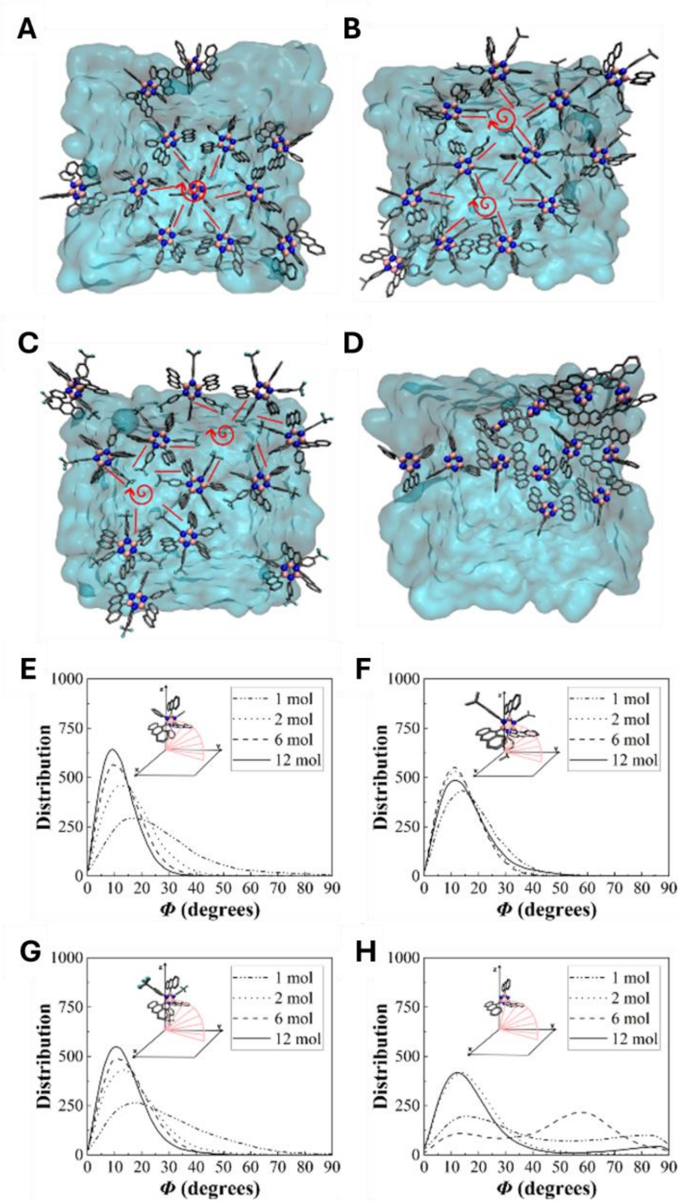

Figure 6.3 Representative MD top-view snapshots of 12 molecules at the air-water interface after equilibration for 10 ns at 300 K. (A), (B), (C), and (D) correspond to borazine **1**, **2**, **3**, and **4**, respectively. The borazines are represented by balls and sticks: boron, carbon, nitrogen, and fluorine are colored in pink, grey, blue, and cyan, respectively; hydrogens are omitted for clarity. The water slab is represented as a light-blue surface. The red bar and spiral arrow indicate either a clockwise or an anticlockwise chiral arrangement above the water surface. (E), (F), (G), and (H) show the distribution of the tilt angle (*Φ*) as

the arc between the plane of the borazine center of each borazine (pink) and the *x-y* plane of the water surface per each borazine system **1**, **2**, **3**, and **4**, respectively, as derived from the MD simulations with 1, 2, 6, and 12 molecules (mol) (see methods section). The tilt angle (Φ) for each borazine is illustrated in the insets. The borazines are represented by balls and sticks: boron, carbon, nitrogen, and fluorine are colored in pink, grey, blue, and cyan, respectively; hydrogens are omitted for clarity. Distribution curves were obtained *via* Gaussian broadening with default standard deviation and normalized per amount of borazine molecules, using a kernel density estimation to produce these plots.

6.2.3 Synthesis and characterization of borazine 2

Borazine **2** was synthesized according to the Wakamiya and co-workers' procedure,[5] with slight modifications. The borazine core was prepared by (1 + 1’ + 1 + 1’ + 1 + 1’) hexamerization of isopropyl aniline and BCl_3. The borazine core was reacted with an excess amount of 9-lithioanthracene to avoid quenching by the formed HCl by-product. **2** was obtained with a 17% yield and characterized using solution NMR, mass spectrometry, elemental analysis, single crystal X-ray diffraction (SCXRD), and solid-state NMR (SS-NMR) (Supporting information, sections 6.5.2 – 6.5.4, and Figure S6.3 – Figure S6.11). We crystallized borazine **2** by slow diffusion of pentane into a solution of borazine **2** in DCM:toluene 1:1 (v/v). In terms of crystal packing characterization, the SCXRD analysis (Table S6.1 – Table S6.2) revealed π-π stacking distances where the anthracene moieties of different borazines **2** are π-π stacked offset face-to-face (OFF) with an average center anthracene-anthracene π-π distance ($D_{center}(C_{anth}\text{-}C_{anth})$) of 3.9–4.8 Å (Figure S6.7). The orientation of the interacting borazines **2** and the π-π stacking distances match the configuration, and the average minimum and center anthracene-anthracene π-π distances of $D_{min}(C_{anth}\text{-}C_{anth}) \approx 3.6$ Å and $D_{center}(C_{anth}\text{-}C_{anth}) \approx 4.6$ Å, respectively, predicted by the MD simulations for the borazine **2**-based film at the water-to-air interface (Figure 6.3B). Larger π-π stacking distances are found in the SCXRD and MD simulations than in the DFT results. This can be explained by the increased cooperative π-π stacking interactions in an aromatic aggregate of multiple borazines **2** compared with the dimer.[14] Moreover, the borazine molecule orientations found in the SCXRD (Figure S6.7) and MD simulation (Figure 6.3B) are similar, with the rigid and non-amphiphilic behavior of the aromatic moieties showing the same hexagonal-based pattern due to stable and oriented OFF π-π stacking interactions among the aromatic groups. Interestingly, when single crystals of borazine **2** were slowly cooled from 203 K down to 110 K in 35–45 min, the distances between the anthracene moieties decreased with a crystal color shift from yellow to white, showing thermochromic properties at low temperatures (Figure S6.7).

To obtain more insights into the π-π stacking interactions between borazine **2** molecules within the crystal, we also performed SS-NMR *via* magic angle spinning (MAS) NMR of the borazine **2** crystals (Supporting information, section 6.5.4, and Figure S6.8 – Figure S6.11). The chemical shifts of the solid-state borazine **2** sample are comparable to those for the molecule in solution, indicating a modest π–π interaction between borazine **2** molecules in the solid state as well as in solution (Table S6.3). The chemical shifts for the molecules in solution and the solid state are listed in Table S6.3, which also shows the DFT theoretical predictions. The standard deviations for the ^{13}C NMR signals between theory and experiments are ≈2.44 ppm and ≈1.82 ppm for the DFT monomer vs. solution NMR (in DCM), and DFT dimer vs. SS-NMR, respectively, demonstrating excellent agreement for the assignment of the NMR signals (Table S6.3). The ^{1}H-^{13}C heteronuclear dipolar correlation MAS NMR experiments provided the ^{1}H resonance assignment of the aromatic moieties of the borazine **2**, allowing probing of the ring currents related to the OFF π–π stacking in the crystal (Figure S6.11).[22] The CH_2 and CH_3 signals on the isopropyl-phenyl moiety at negative ppm values are evidence of cooperative aggregation in aromatic OFF π–π stacking packing.[22] The borazine **2** crystal MAS NMR shows upfield aggregation shifts for the CH_2 and CH_3 isopropyl signals (Figure S6.11), confirming the presence of cooperative π–π stacking interactions in OFF packing. The splitting of the CH_2 and CH_3 isopropyl MAS NMR signals is further confirmed by the SCXRD analysis at 203 K, which reveals that two out of the three isopropyl groups are disordered. The carbons of these two isopropyl groups exist in two different orientations with specific occupancy factors of 0.70 vs. 0.30 (for carbons C27/C28/C29), and 0.47 vs. 0.53 (for carbons C37/C38/C39), respectively, as extracted from the crystallographic data (Table S1). Overall, this is in line with the OFF packing found in the DFT and MD simulations.

6.2.4 Langmuir-Blodgett film fabrication, surface-tension results, and Langmuir-Blodgett-like MD simulations

When preparing Langmuir-Blodgett films it has been reported that the solute concentration of non-amphiphilic molecules can strongly affect film morphology.[23–25] To investigate the behavior of non-amphiphilic borazine **2**, different stock solutions of borazine **2** were prepared in chloroform ($CHCl_3$), ranging from 0.5 mg mL^{-1} to 0.05 mg mL^{-1}. These solutions were then carefully spread at the water-to-air interface at room temperature, and the chloroform was allowed to evaporate (Figure 6.4A). The total amount of deposited borazine **2** on the water-to-air interface remained the same (23 nmol), while the total amount of chloroform changed from

44 µL to 440 µL to accommodate the different stock concentrations. After evaporation of chloroform, we initiated the compression of the Langmuir film in the Langmuir-Blodgett trough (Figure 6.4B), during which the surface pressure in mN m^{-1} and mean molecular area (MMA) in $Å^2$ $molecule^{-1}$ ($Å^2$ $molec^{-1}$) were monitored to record the compression isotherms (Figure 6.4C, Figure S6.12, and Figure S6.13A). Depending on the concentration of the starting stock solution, the compression produced different isotherms. The change in concentration does not affect the isotherm of amphiphilic molecules such as 1-palmitoyl-2-oleoyl-sn-*glycero*-3-phosphocholine (POPC) (Figure S6.13B) taken as an amphiphilic standard, suggesting that the shift in the isotherm for the borazine **2** system is due to the non-amphiphilic characteristics of borazine. We hypothesized that the difference in isotherms is caused by aggregation during the deposition step on water (Figure 6.4A); it has been reported that the spreading of similar anthracene molecules at the water-to-air interface displayed immediate crystal formation upon evaporation of the solvent.[16] In our experiments, while the total amount of deposited borazine **2** remains the same, the amount of borazine **2** per droplet (and the number of droplets) depended on the concentration of the stock solution. The use of more concentrated solutions results in deposition of higher amounts of borazine **2** per droplet at the surface, which are more prone to aggregation before the molecule could spread and equilibrate at the surface.[16] Therefore, by lowering the concentration of the stock solution, we minimized aggregation of borazine **2** during deposition. This effect can be observed by the shift of the isotherm toward higher MMA values at lower concentrations (Figure 6.4C), allowing the formation of increasingly homogeneous films on the water's surface (see section 6.2.5). The tangent line drawn at 2 mN m^{-1} on the experimental green isotherm (Figure 6.4C) indicates the MMA corresponding to the film morphology after the compression is released during the transfer onto the silicon wafer, Si/SiO_2 (Figure 6.4B).[26]

The surface pressure variation in the Langmuir-Blodgett experimental setup can be simulated *via* a computational approach consisting in applying pressure in the *x-y* plane of the simulation box.[15] Constant surface pressure simulations for six pressure values were performed for 12 molecules of borazines **2** on the water slab; each calculation was repeated three times to improve statistics. Plotting surface pressure vs. mean molecular area (MMA) yields an isotherm that enables direct comparison to the experimental data (Figure 6.4C). This calculation afforded computed isotherms that were comparable with experimental isotherms, apart from a constant offset (Figure 6.4C). Comparing MMAs at a surface pressure of 2 mN m^{-1} provides an estimate of about 19 $Å^2$ for this offset. This value can be explained by the presence of a uniform distribution of borazine **2** monomers in one monolayer above the water slab at the beginning of the compression simulations (see Figure 6.4D), while most likely the experimental distribution of borazine **2** at the interface of the water surface before compression is heterogeneous. In particular, experimentally, initial aggregation can lead to the formation of sporadic cluster islands, which will decrease the MMA compared to the MMA for dispersed molecules. This interpretation is further supported by the finding that the slopes at a surface pressure of 2 mN m^{-1} for the experimental and computational isotherms are comparable, −0.30 mN molec m^{-1} $Å^{-1}$ and −0.28 mN molec m^{-1} $Å^{-1}$, respectively, suggesting the π-π stacking and packings are similar to each other and, consequently, mechanical properties such as elasticity are similar as well.[26] In the MD simulations, the thickness of the borazine **2**-based film before compression (without surface pressure) is approximately 1 nm and corresponds to a monolayer of borazine **2** molecules (Figure 6.4D). With the gradual increase of the surface pressure, the average thickness doubled with respect to no surface pressure, as shown in Figure S6.14 by the density peaks of the borazine **2** molecules within the simulation box. For a surface pressure of 2 mN m^{-1}, the average thickness increases to approximately 2 nm, which corresponds to the formation of a bilayer of borazine **2** (see Figure 6.4E). This result is further confirmed by the peak in the density of the borazine **2**-based film that doubled in width in the 2 mN m^{-1} case with respect to the one without surface pressure (Figure S6.14). In the case of a surface pressure of 2 mN m^{-1}, the OFF π-π stacking between the anthracene moieties is retained (Figure 6.4C, circle snapshot) within the bottom layer. Specifically, in the MD simulation at a surface pressure of 2 mN m^{-1}, the anthracene moieties exhibit characteristic OFF π-π stacking arrangements, with approximate average minimum and center anthracene-anthracene π-π distances of $D_{min}(C_{anth}\text{-}C_{anth}) \approx 3.5$ Å and $D_{center}(C_{anth}\text{-}C_{anth}) \approx 4.8$ Å, respectively, within the bottom layer. We highlight the presence of interactions between borazine **2** among the bottom and top layers (see Figure 6.4C solid circle snapshot, and Figure 6.4E). This interaction shows a typical OFF π-π stacking fashion between the lower part of the anthracene moieties of the top layer and the upper part of the anthracene moieties of the bottom layer (see Figure 6.4C solid circle snapshot and Figure 6.4E). The approximate average minimum and center anthracene-anthracene π-π distances among layers are $D_{min}(C_{anth}\text{-}C_{anth}) \approx 3.5$ Å and $D_{center}(C_{anth}\text{-}C_{anth}) \approx 5.6$ Å, respectively. As a consequence of the applied surface pressure, we observed a partial reorientation of the borazine **2** molecules above the water surface (Figure 6.4E), indicated by the slight shift in the tilt angle from 10°-15° of the uncompressed system to ≈ 20-25° of the one at a surface pressure of 2 mN m^{-1} (Figure S6.15). This rearrangement under compression is attributed to the OFF π-π stacking interactions among the anthracene moieties of the bottom and top borazine **2** layers (Figure 6.4C-E). The overall stability of the organized pattern under the Langmuir-Blodgett-like condition is attributed to the persistent OFF π-π stacking acting as a cooperative-oriented driving force between anthracene groups, outlining an entropy-harnessing effect along with the intrinsic rigidity of borazine **2**.[27–29]

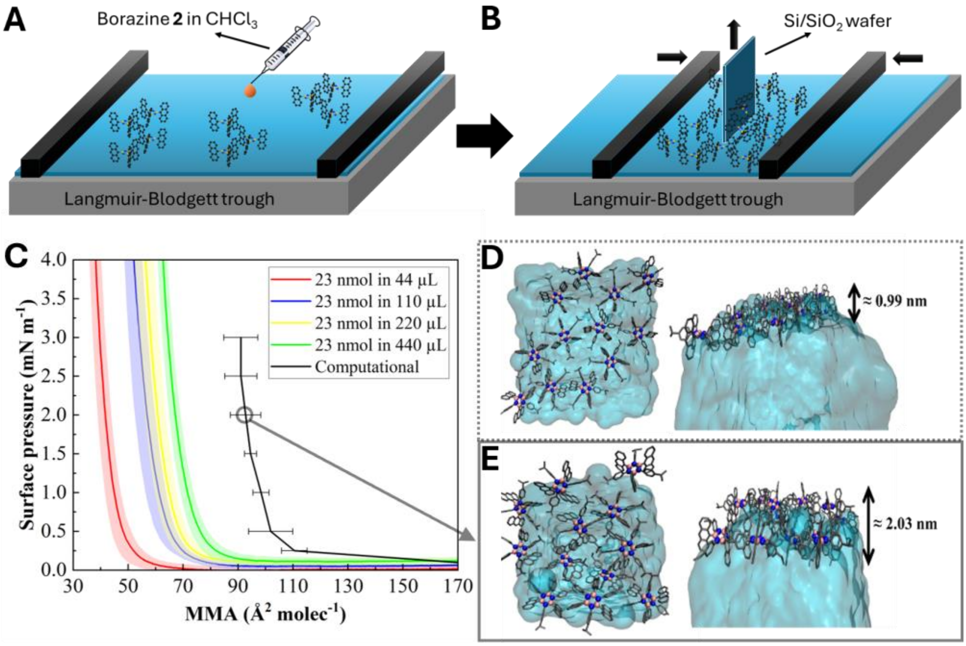

Figure 6.4 Experimental and computational study of borazine 2 deposited on a water surface. (A) Illustration of a Langmuir–Blodgett trough. A range of 0.5 to 0.05 mg mL^{-1} solutions of borazine **2** in chloroform were deposited dropwise at the water-to-air interface. (B) Illustration of a Langmuir–Blodgett trough after compressing the borazine **2** molecules above the water surface, and subsequent transfer by the Langmuir-Blodgett method of the thin film onto a silicon wafer (Si/SiO$_2$) brought into contact with the compressed borazine **2** molecules. (C) Langmuir–Blodgett isotherms of the borazine **2** thin film after depositing 23 nmol borazine **2** dissolved in increasing amounts of CHCl$_3$ (from 44 µL to 440 µL), where the surface pressure in mN m^{-1} is plotted vs. the mean molecular area (MMA) in Å^2 molec^{-1}. The lighter-colored areas indicate the standard deviation for each corresponding isotherm from two to four replicates (see methods section). Upon dilution, the isotherm is shifted to higher MMA. The intersection of the extrapolated violet dashed line with the point of tangency with the green isotherm (23 nmol in 440 µL) at 2 mN m^{-1} indicates the MMA at which corresponds the morphology of a homogeneously distributed film. The solid black line is the isotherm computed *via* MD simulations under Langmuir-Blodgett-like conditions for a system of 12 molecules of borazine **2**. The MMA is averaged over three separate MD simulations with error bars indicating standard deviations. (D) Top and side views of 12

molecules of borazine **2** at the water-air interface after MD equilibration without surface pressure at 300 K. (E) Top and side views of 12 molecules of borazine **2** after MD compression at 2 mN m^{-1} surface pressure (black circle in panel C) and 300 K. Packing of borazine **2** has a hexagonal-based pattern structure at the water-air interface involving all the anthracene moieties stacked in an offset face-to-face (OFF) configuration, consistent with the crystal structure reported in Figure S6.7. The thickness (black bifrontal arrows in panels D and E) for each system of borazine **2** fluctuates between 0.99 nm for the system without surface pressure and around 2.03 nm for the Langmuir-Blodgett-like system at 2 mN m^{-1} surface pressure, indicating monolayer and bilayer assemblies, respectively. Borazine **2** is represented by balls and sticks: boron, carbon, nitrogen, and fluorine are colored in pink, grey, blue, and cyan, respectively, and hydrogens are omitted for clarity.

6.2.5 Langmuir-Blodgett film thickness analysis *via* AFM and freestanding ability *via* SEM

The borazine thin films were formed from diluted solutions of borazine **2** in $CHCl_3$ and subsequently compressing them in a Langmuir-Blodgett trough at different surface pressures (Figure 6.4C and Figure S6.13A). The floating films were transferred onto the Si/SiO_2 substrate using the Langmuir-Blodgett technique. Large uniform films were found spanning areas of over 100 × 100 μm for those obtained at 2 mN m^{-1} surface pressure (Figure 6.4C green line, Figure 6.5A, Figure S6.16, and Figure S6.17A). Atomic force microscopy (AFM) was used to determine the average film thickness by analyzing the height profile over a crack in the film (Figure 6.5A). These uniform thin films show a thickness of 2.1 nm, corresponding to a bilayer of borazines **2** (Figure 6.5B). This value aligns well with the thickness extracted from the MD simulations for borazine **2** at 2 mN m^{-1} (Figure 6.4E). Then, we compared the Langmuir-Blodgett films obtained from 0.05 mg mL^{-1} at two different surface pressures: 2 vs. 15 mN m^{-1}. Although the flakes obtained at 15 mN m^{-1} surface pressure showed a thickness of 2.2 nm, they exhibited high degrees of aggregation (Figure S6.18). This can be attributed to the presence of inhomogeneous clusters, characterized by elevated height levels observed in the AFM (Figure S6.18). The borazine **2** molecules form a uniform bilayer at a low surface pressure of 2 mN m^{-1}, and eventually collapse into multi-layered films with inhomogeneous aggregates upon further compression at 15 mN m^{-1}. To avoid aggregate formation, all production transfers were performed at 2 mN m^{-1}. Afterward, we compared the quality of the films obtained from two different stock concentrations: 0.05 vs. 0.2 mg mL^{-1}. By changing the stock concentration from 0.05 to 0.2 mg mL^{-1}, flakes spanning areas of 20 × 20 μm could be transferred with a similar thickness of 1.8 nm (Figure S6.19). However, larger particles could be observed in the 0.2 mg mL^{-1} case, characterized by bright spots in the AFM, resulting in the production of borazine **2**-based film with a smaller area due to a less stable morphology of the film compared to the 0.05 mg mL^{-1} case. Although the thickness remains similar to the 0.05 mg mL^{-1} case, the overall quality of the Langmuir-Blodgett films derived from the higher concentration stock at 0.2 mg mL^{-1} appears reduced. Finally, to investigate whether the transfer speed on the Si/SiO_2 substrate affects the resulting films, we analyzed films obtained from 0.05 mg mL^{-1} at a fast transfer speed of 2.5 mm min^{-1} (Figure S6.20), compared to 0.5 mm min^{-1} (Figure 6.5A-B). At the faster transfer speed, the films were thinner and contained many holes and clusters characterized by the bright spot in the AFM (Figure S6.20). We investigated the thickness by analyzing the cross-section of the edge of the flake, which revealed a value of approximately 1 nm. This thickness corresponds to a monolayer borazine **2**-based film. The fast transfer produced flakes smaller than 100 × 100 μm observed at a slower transfer speed of 0.5 mm min^{-1} (Figure 6.5A and Figure S6.17A). Therefore, we hypothesize that a stable and uniform Langmuir-Blodgett borazine **2**-based film forms as a bilayer at 2 mN m^{-1} surface pressure, 0.05 mg mL^{-1} stock concentration, and transfer speed onto the Si/SiO_2 substrate of 0.5 mm min^{-1}.

To investigate the freestanding ability of the borazine **2**-based film, the Langmuir-Blodgett films created from 0.05 mg mL^{-1} borazine **2** in $CHCl_3$ and compressed to 2 mN m^{-1} were transferred *via* the Langmuir-Schaefer technique onto copper transmission electron microscopy (TEM) grids covered with QUANTIFOIL containing 0.6 μm apertures. These borazine **2**-based films were found to be freestanding over 0.6 μm holes (Figure 6.5C). However, when these films were exposed to the electron beam in the scanning electron microscopy (SEM), holes appeared and grew larger in the films during the measurements (Figure S6.17B). We could not detect long-range crystallinity of the Langmuir borazine **2**-based film by selective area electron diffraction (SAED) (Figure S6.17C), presumably due to electron beam damage. To confirm that these holes are only formed during measurement and not during sample fabrication, AFM tapping mode was used on transferred samples before SEM measurements. Intact and stable freestanding films could be found over 0.6 μm holes (Figure 6.5D and Figure S6.17D). In conclusion, consistent with the previous study on decacyclene-based Langmuir-Blodgett films,[15] these results demonstrate that the intermolecular cooperative π-π stacking interactions between the aromatic moieties in the borazines **2**, anthracenes and isopropyl-phenyls, are sufficiently strong to render the borazine **2**-based bilayer film freestanding over 0.6 μm areas.

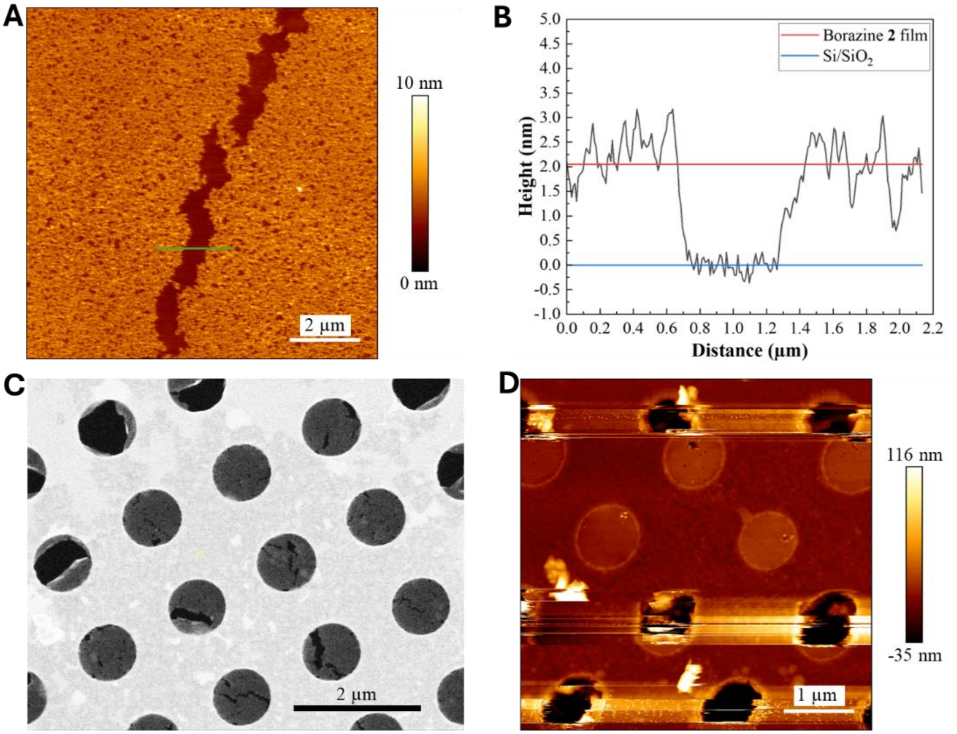

Figure 6.5 Thickness and freestanding ability analysis of the borazine 2 thin films after transfer. (A) The magnification to 10 × 10 μm of a crack in the Langmuir-Blodgett film is measured *via* AFM, (B) the cross-section was plotted over the green bar in panel A, resulting in an estimated height of 2.1 nm calculated by the height difference between the average of the borazine and the Si/SiO$_2$ heights. (C) SEM image collected at 25000× magnification (black scale bar, 2 μm) shows the Langmuir-Schaefer films prepared from 0.05 mg mL^{-1} solution, compressed to 2 mN m^{-1}, on a QUANTIFOIL carbon film perforated with an array of 0.6 μm diameter holes on a copper TEM grid. (D) The AFM analysis of Langmuir-Schaefer free-standing film obtained from 0.05 mg mL^{-1} solution, compressed to 2 mN m^{-1}, on QUANTIFOIL containing 0.6 μm diameter holes (violet bar) on a copper TEM grid before the SEM. The AFM analysis of the freestanding area (magnified) is reported in Figure S6.17.

6.2.6 Molecular orientation *via* UV-Vis and fluorescence spectroscopy

To confirm the packing mode of the borazine **2** molecules retained in the Langmuir-Blodgett films, UV-Vis absorption and fluorescence spectroscopies were employed to measure absorption and fluorescence on the borazine **2**-based films transferred onto quartz. Compared to borazine **2** in the solution of CHCl$_3$ with a maximum absorbance ($A_{max,solution}$) at 392 nm, a slightly redshifted but similar absorption spectrum was observed for the Langmuir-Blodgett borazine **2**-based film with a maximum absorbance ($A_{max,LB}$) at 400 nm (Figure 6.6A). This slight redshift in the absorption spectrum is an indication of overlapping anthracene moieties.[16,30,31] On the other hand, fluorescence experiments on the Langmuir-Blodgett borazine **2**-based film revealed a large redshifted broad signal with a maximum emission intensity ($I_{max,LB}$) at 485 nm, with no detectable vibronic features associated with isolated anthracenes (Figure 6.6B). This broad signal is attributed to anthracene excimer formation in the solid state, which is typically broad, featureless, and significantly red-shifted relative to the well-defined vibronic emission of free, non-interacting anthracene units.[32] The occurrence of excimer emission is a reliable indication of interaction among anthracene moieties, reinforcing the idea of having the OFF (offset face-to-face) π-π stacking.[16,30,31,33] In addition, the wavelength of solid-state anthracene excimer signals correlates with the overlap ratio between the two anthracene monomers, with an excimer peak around 489 nm for the borazine **2**-based film corresponding to an overlap of approximately 30%.[33] Interestingly, the redshift in absorption and fluorescence spectra was also observed in the borazine **2**-based layer prepared by spin-coating from a solution of borazine **2** in $CHCl_3$ on quartz (Figure 6.6A-B), indicating that borazine **2** rapidly self-assembles into an OFF π-π stacking motif. Consequently, the incorporation of poly(methyl methacrylate) (PMMA) to physically separate the borazine **2** during spin-coating leads to the absence of the excimer emission (Figure 6.6B). Moreover, the UV-Vis absorption and fluorescence spectra in $CHCl_3$ were further analyzed *via* time-dependent DFT (TD-DFT) calculations in the polarizable continuum model (PCM) for $CHCl_3$ solvation, and vibrationally resolved spectra were computed using the FCclasses3 program (Figure S6.21), showing a remarkable confirmation of the experimental data in $CHCl_3$ solution.[34] In summary, UV-Vis measurements on the borazine **2**-based film, consistent with DFT calculations, MD simulations at the water-to-air interface, and in agreement with SCXRD and SS-NMR data, confirm the strong π-π stacking tendency of borazine **2** and its likely adoption of an OFF (offset face-to-face) stacking motif in both the crystal and the film. This corresponds to a borazine **2** hexagonal gear-shaped conformation in the crystal, which is expected to translate to a hexagonal-based pattern in the film.

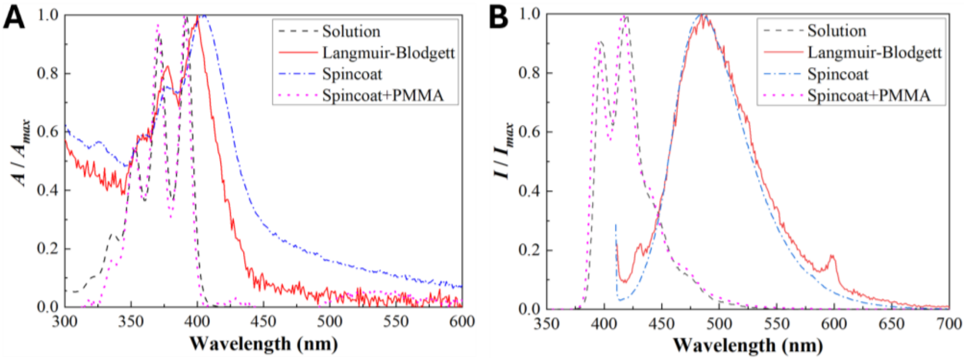

Figure 6.6 Absorption and fluorescence spectra of borazine 2 in $CHCl_3$ and borazine 2 films on quartz. (A) UV-Vis absorption spectra plotting the absorbance (A) scaled to their maximum absorbance (A_{max}) vs. wavelength in nm. (B) Fluorescence spectra plotting the emission intensity (I) scaled to their maximum emission intensity (I_{max}) vs. wavelength in nm. The black dashed line represents borazine **2** in solution (50 µM in $CHCl_3$) ($A_{max,solution}$ = 1.26 (392 nm), $I_{max,solution}$ = 41467 a.u. (420 nm)). The red solid line represents the Langmuir-Blodgett borazine **2**-based film on quartz prepared from 0.05 mg mL^{-1} in $CHCl_3$, compressed to 2 mN m^{-1} and transferred with a speed of 0.5 mm min^{-1} ($A_{max,LB}$ = 0.012 (400 nm), $I_{max,LB}$ = 7105 a.u. (485 nm)). The blue dash-dotted line represents the spin-coated layer of borazine **2** (1 mg mL^{-1} in $CHCl_3$, 80 µl, 500 rpm, 1 min) ($A_{max,spincoat}$ = 0.052 (405 nm), $I_{max,spincoat}$ = 182965 a.u. (486 nm)). The magenta dotted line represents the spin-coated layer of borazine **2** (1 mg mL^{-1} in $CHCl_3$) diluted (1:1 v/v) with PMMA (600 kDa, 0.4 µM in anisole) (80 µL, 500 rpm, 2 min) ($A_{max,PMMA}$ = 0.026 (391 nm), $I_{max,PMMA}$ = 352078 a.u. (416 nm)).

6.3 Conclusions

In this study, we develop and present a combined computational–experimental strategy to design and realize the first borazine-based, molecular-thick free-standing film, assembled *via* the Langmuir–Blodgett method. Using a step-wise multiscale computational approach of DFT and All-Atom MD simulations, borazine **2** was identified as the most promising candidate among four screened borazines due to its favorable π–π stacking energetics and stable hexagonal packing at the water-to-air interface. Experimental validation confirmed the successful synthesis and Langmuir-Blodgett assembly of borazine **2** into uniform bilayer films, with AFM-measured thickness (≈ 2.1 nm) in full agreement with MD predictions. Fluorescence spectroscopy of the film revealed excimer emission consistent with offset face-to-face π–π stacking, as also observed in the crystal structure by SCXRD and SS-NMR. These findings confirm that the self-assembly motif is preserved from crystal to film and is driven by directional π–π interactions. Despite minor limitations in crystallinity and electron beam stability, the films exhibited sufficient cohesion to span 0.6 μm apertures, confirming their freestanding nature. This work provides a proof of concept for the rational design and fabrication of 2D boron-nitride-rich organic nanomaterials based on borazine molecules driven solely by π-π stacking interactions. Future work could explore functionalized or amphiphilic derivatives to enhance ordering and stability, or introduce covalent locking strategies such as photopolymerization.[14,16] Overall, this study lays the groundwork for tunable, π-stacked thin-film materials with potential applications in tunable nano(opto)electronics technologies such as organic light-emitting diodes (OLEDs), and energy storage devices.

6.4 Computational and experimental section

Calvani, D., Buda, F., de Groot, H. and Sevink, A. performed and analyzed all the computational studies (DFT-based and MD simulations) and the experimental SS-NMR study.

6.4.1 Computational methods: DFT calculations

Geometry optimization of the borazine **1**, **2**, **3**, and **4** molecules (monomers) in the gas phase was performed using the DFT method with the PBE0 functional,[35,36] D3(BJ) correction,[37] and 6-31G(d,p) basis set, using the Gaussian 16 program suite.[38] To assess the contributions of π-π stacking within the borazines, geometry optimizations were conducted for dimers of identical borazine **1**, **2**, **3**, and **4** molecules using the same level of calculation employed for the monomers. The π-π stacking interaction for each dimer was approximated by subtracting twice the energy of the monomer from the total energy of the dimer, and then dividing this energy difference by the number of carbon atoms within the three anthracene groups (totaling 42 carbon atoms). These anthracene groups predominantly engage in the π-π stacking interaction energy.[17] This interaction energy ($\Delta E/N$) is calculated using the formula: $\Delta E/N = (E_{\text{dimer}} - 2 \cdot E_{\text{monomer}})/N$, as presented in Figure 6.2.

To compute the energy variation associated with changing the C-C-B-N dihedral angle in each borazine monomer (Figure S6.2), a series of DFT scans of one representative C-C-B-N dihedral angle was performed. These scans utilized the PBE0 functional,[35,36] D3(BJ) correction,[37] and 6-31G(d,p) basis set implemented through the Gaussian 16 program suite.[38]

To compute the NMR chemical shifts of the borazine **2** (Table S6.3) single points calculations on the optimized monomer and dimer structures were performed at density functional theory (DFT) level with the PBE functional,[39] D3(BJ) correction,[37] and TZP basis set, using AMS software.[40]

6.4.2 Computational methods: all-atom MD simulations of the water slab

All MD simulations were carried out using the GROMACS 2021 software suite.[41–47] The Particle Mesh Ewald method was employed to accurately account for electrostatic interactions.[48] The cut-off for Coulomb and Lennard-Jones interactions was set to 10 Å. During the NVT simulation, the temperature was kept fixed with the V-rescale coupling method.[49]

The model for the water slab, comprised of 4139 water molecules, was simulated in a periodic box 5.0 × 5.0 × 20.0 nm^3 using the TIP4P-Ew/2004 force field.[50] The water surface tension was used as defined within the GROMACS software suite according to

$$\gamma_{\text{water}} = \frac{1}{2} L_z \left[P_{zz} - \frac{1}{2}(P_{xx} + P_{yy}) \right],$$

where L_z is the box length in the z-direction, P_{xx}, P_{yy} and P_{zz} are the respective xx, yy and zz elements of the pressure tensor,[51] and the ½ originates from the presence of two x-y plane surfaces in the system. The system was first energetically minimized and then equilibrated for 8 ns with NVT at 300 K to obtain an average surface tension of γ_{water} = 58.46 mN/m. This value is in good agreement with previous studies.[52,53] The water model was further validated using a radial distribution function and density analysis.[15] Borazines **1**, **2**, **3**, and **4** were simulated using the All-Atom Optimized Potential for Liquid Simulations (OPLS-AA) force field,[54–56] with parameters calculated *via* the LigParGen[57] parameterization tools and for the central borazine ring obtained by reference boron-nitride OPLS-AA parameter.[58] Partial charges were calculated with the CM5 model,[59] and derived from single points calculations on the optimized borazine **1**, **2**, **3**, and **4** monomer structures performed at density functional theory (DFT) level with the PBE0 functional,[35,36] D3(BJ) correction,[37] and 6-31G(d,p) basis set, using Gaussian 16 program suite.[38] All MD results were illustrated using Visual Molecular Dynamics (VMD).[60] The OPLS-AA parameters for borazine **1**, **2**, **3**, and **4** are reported in the Data Availability section.

6.4.3 Computational methods: all-atom MD simulations of the borazines at water-air interface and under Langmuir-Blodgett-like conditions

Random input positions of 1, 2, 6, or 12 borazine molecules in a range of 10 Å above both water surfaces were generated using the PACKMOL18 program.[61] Having two independent water-borazine interfaces provides a more symmetric MD simulation box and increases the statistics of the results by averaging over both interfaces compared to having only one water-to-borazine interface. Moreover, the presence of the borazines on both sides avoids the diffusion of the water molecule through the periodic boundary condition along the *z*-axis. The two interfaces can be considered independent due to the 5 nm thickness of the water box and a vacuum space of at least 5 nm above both the borazine molecules distributions along the *z*-axis (Figure S6.22). For each simulation, the system was first equilibrated with NVT simulation at 70 K for 5 ns, and the temperature was then raised to 300 K for another 5 ns of NVT simulation. After these equilibrations, the production MD consisted of an NVT simulation run at 300 K for 10 ns. The final configuration extracted from the production MD was used as a starting point for the subsequent NPT surface tension simulations. This independent series of MD simulations was run for each borazine system, **1**, **2**, **3**, and **4** (Figure 1). Data presented in the manuscript were obtained by averaging the values on the final 10 ns of each corresponding production MD simulation (Figure 6.3).

For 12 molecules of borazine **2**, surface tension MD simulations were performed, using a surface tension coupling for surfaces parallel to the *x*-*y* plane. It employs normal pressure coupling for the *z*-direction. The surface pressure was then increased stepwise to generate the surface pressure vs. MMA isotherm. At each chosen surface pressure (0, 0.25, 0.5, 1, 1.5, 2, 2.5, 3 mN m^{-1}), the surface tension coupling molecular dynamics has been performed while monitoring the change of the area in the *x*-*y* plane. To execute the constant surface tension simulations, Berendsen pressure coupling was used.[15,43] For this coupling method to be effective, a value for the compressibility is required, which is close to the real compressibility of the system, namely 4.5×10^{-5} bar^{-1}.[62] Simulations were stopped after 10 ns, at which point an equilibrium state was reached. We ran three independent production MD simulations for each chosen surface pressure (0, 0.25, 0.5, 1, 1.5, 2, 2.5, 3 mN m^{-1}). Data presented in the manuscript was obtained by averaging the values on the total 10 ns of each corresponding production MD simulation at each surface pressure

(Figure 6.4). The slope for the theoretical isotherm at 2 mN m^{-1} was determined using linear regression on data points ranging from 1.5 and 2.5 mN m^{-1}.

6.4.4 Computational methods: DFT and TD-DFT simulations of absorption and fluorescence spectra

The DFT and TD-DFT calculations for the absorption and fluorescence spectra on the borazine **2** (Figure S19) were conducted using the CAM-B3LYP functional,[63] D3(BJ) correction[37] and 6-31G(d,p) basis set, following previous benchmarking on similar molecules. These calculations were performed employing the Gaussian 16 program suite.[38] We computed the lowest three singlet excited states, which cover excitations up to approximately 3.54 eV, encompassing the full relevant UV-Vis range observed experimentally. The ground state and excited state geometries, and the corresponding vibrational frequencies, have been determined at DFT and TD-DFT levels, respectively, including implicit continuum solvent effects for the $CHCl_3$ with the PCM scheme.[64] Starting from the calculated harmonic vibrational spectra of the ground state and excited state, the vibrationally resolved spectra were computed using the FCclasses3 program.[34] This computation employed a time-dependent (TD) approach that is eigenstate-free, relying on the fast evaluation of the analytical expressions for the time-correlation functions and their Fourier transform.[34] The reported spectra have been simulated using convoluting Lorentzian functions presenting a half-width at half-maximum (HWHM) that has been adjusted to allow meaningful comparison with experiments (0.021 eV).[34] FCclasses3 is one of the most effective codes for computing vibrationally resolved spectra; it uses the Franck-Condon approximation,[65,66] and selects only the relevant vibronic contributions. It is mostly applied within the harmonic approximation for both initial and final states. In this case, an adiabatic (AH) scheme has been used,[67] that expands the potential energy surface (PES) of the final state around its equilibrium geometry.

6.4.5 Experimental methods: synthesis of borazine 2

Borazine **2** was synthesized according to the literature,[5] with minor alterations. 4-isopropyl aniline (0.190 mL, 1.41 mmol, 1 eq) in dry, degassed toluene (2 mL) was added dropwise to a solution of BCl_3 in heptane at 0 °C in a flame-dried Schlenk flask under a constant flow of N_2. The solution was refluxed and stirred overnight. Purging and freeze-pump-thawing were not sufficient for the complete removal of the formed HCl. The mixture was then added to a solution containing an excess amount of 9-lithioanthracene at 0 °C, which was prepared from 9-bromoanthracene (1.60 g, 6.22 mmol, 4.4 eq) and t-BuLi (7.3 mL, 12.4 mmol, 8.8 eq, 1.7 M in pentane) in THF (12 mL) at -78 °C under N_2. The mixture was allowed to warm to RT and was stirred overnight. Then, water was added (5 mL), and an aqueous layer was extracted with $CHCl_3$ (3 × 10 mL). The combined organic layer was dried with $MgSO_4$, filtered, and evaporated under reduced pressure. The trianthryl-substituted borazine **2** was purified using silica column chromatography (toluene in pentane 40% → 100%). The slow diffusion of pentane into a solution of borazine **2** in toluene or DCM yielded the product as yellow crystals (78 mg, 0.081 mmol, 17%). ^{1}H NMR (400 MHz, $CDCl_3$) δ 8.39 (dd, J = 8.6, 1.0 Hz, 6H), 7.94 (s, 3H), 7.68 (dd, J = 8.0, 0.9 Hz, 6H), 7.55 (ddd, J = 8.6, 6.6, 1.3 Hz, 6H), 7.30 (ddd, J = 8.4, 6.6, 1.1 Hz, 9H), 6.51 (d, J = 8.4 Hz, 6H), 5.77 (d, J = 8.3 Hz, 6H), 2.00 (heptet, J = 6.9 Hz, 3H), 0.46 (d, J = 6.9 Hz, 18H). ^{13}C NMR (101 MHz, $CDCl_3$) δ 144.0, 142.8, 137.7, 133.1, 130.8, 129.6, 128.6, 126.6, 126.3, 124.43, 124.36, 123.9, 32.8, 23.3. ESI MS m/z 963.5 (M^+). HR-MS m/z 964.5, 981.5 ($M+H^+$, $M+NH_4^+$). Anal. Calcd for $C_{69}H_{60}B_3N_3$: C, 86.00; H, 6.28; N, 4.36. Found: C, 85.91; H, 6.29; N, 4.34. See section 6.5.2 and Figure S6.3 – Figure S6.6 in the Supporting information for more details.

6.4.6 Experimental methods: characterization of borazine 2

The borazine **2** was characterized by NMR, mass spectrometry, elemental analysis, SCXRD, and SS-NMR (Supporting information, sections 6.5.2 – 6.5.3). Liquid-state NMR measurements (Figure S6.9) were performed on a Bruker Avance-III-HD 850 MHz standard bore liquid-state NMR spectrometer with a 19.96 Tesla magnetic field. In this field, ^{13}C and ^{1}H resonate at 213.84 and 850.33 MHz, respectively. A 5 mm cryoprobe (type CPTCI ^{1}H-^{13}C/^{15}N/D) with a Z gradient system was used. The 90-degree pulses used for the proton and carbon experiments were 8.8 and 12 microseconds at 10 W and 135 W. A 5 mm NMR tubes (Z172600) were purchased from Cortecnet. Deuterated solvents were purchased from Eurisotop.

SS-NMR measurements (Figure S6.10 – Figure S6.11, and Table S6.3) were performed with a Bruker Neo console 750 MHz wide bore SS-NMR spectrometer in a 17.6 Tesla magnetic field. In this field, ^{13}C and ^{1}H resonate at 188.66 and 750.23 MHz, respectively. A standard 3.2 mm triple resonance E-free MAS probe was used. All the samples were packed in 3.2 mm thick-walled zirconium rotors with vessel caps and were spun around the magic angle (54.74) at spinning frequencies of 15 or 20 kHz. The temperature was kept constant at 298 K.

6.4.7 Experimental methods: preparation and deposition of Langmuir films

Langmuir films were prepared with a KSV NIMA instrument equipped with a Teflon Langmuir trough (24300 mm^2), Delrin barriers, a platinum Wilhelmy plate, and a dipper, using Milli-Q water as the subphase. Varying concentrations of **2** in $CHCl_3$ were prepared by diluting an initial stock solution of 1 mg mL^{-1} with $CHCl_3$ until the desired concentration. The spreading of the borazine **2** in $CHCl_3$ solution was performed by carefully approaching the water surface with droplets hanging from the airtight glass syringes until physical contact. After 20 min, compression was started at a rate of 2 mm min^{-1} until the desired surface pressure was reached and maintained for 15 min. Langmuir films were transferred onto Si/SiO_2 and quartz substrates *via* the Langmuir-Blodgett method by slowly pulling the substrate (typically 1 × 2 cm) upwards vertically (0.05 mm min^{-1} unless specified otherwise) from the subphase at constant surface pressure. Langmuir films were transferred onto copper/QUANTIFOIL TEM grids *via* the Langmuir-Schaefer method. See also Supporting information section S4 for more details. The slope for the experimental isotherm at 2 mN m^{-1} was determined using linear regression on data points ranging from 1.5 and 2.5 mN m^{-1}.

6.4.8 Experimental methods: characterization of borazine 2-based films

AFM was performed using a PK Nanowizard 4 Ultra Speed AFM. Height analysis was performed in AC mode on Langmuir-Blodgett films deposited on Si/SiO_2 wafers using tips with a resonance frequency of 300 kHz and a spring constant of 26 mN m^{-1}. Samples on Cu/QUANTIFOIL TEM grids were measured using tips with a resonant frequency of 70 kHz and a spring constant of 2 mN m^{-1}. SEM was measured on an Apreo SEM instrument equipped with a CCD camera. Typical imaging conditions were a T2 detector with the Optiplan Use case, an acceleration voltage of 2 kV, and a beam current of 13-100 pA. TEM experiments were conducted on a Talos L120C (Thermo Fisher Scientific) microscope operated at 120 kV. UV-Vis spectroscopy was performed on a Cary 60 (Agilent) instrument. Fluorescence spectroscopy was performed with an FLS900 fluorescence spectrometer equipped with a 450 W Xenon lamp. Solutions were measured in a quartz cuvette cell with a path length of 1 cm. Langmuir-Blodgett and spin-coated films were measured on a quartz slide.

6.5 Supporting information

6.5.1 Computational Results

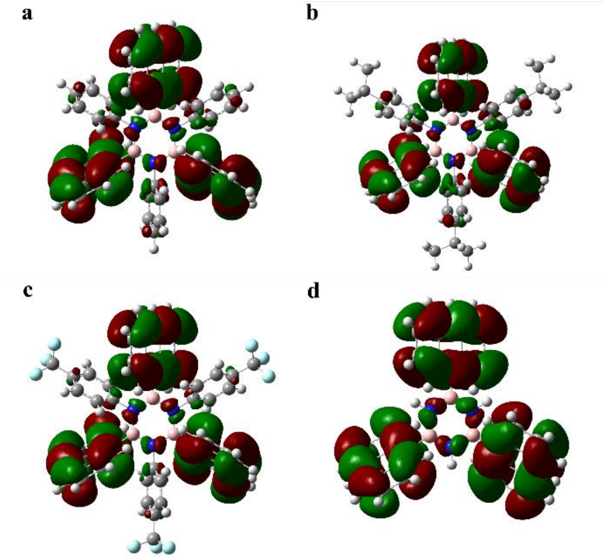

Figure S6.1 Geometry optimized monomer configurations and pictorial representations of the KS HOMO for each type of borazine. Panels **a**, **b**, **c**, and **d** represent borazine **1**, **2**, **3**, and **4**, respectively, with isosurface value = 0.01 (Figure 6.1 in the main text). In ball and stick the molecular structures, with hydrogens in white, boron in pink, carbon in grey, nitrogen in blue, and fluorine in cyan, respectively.

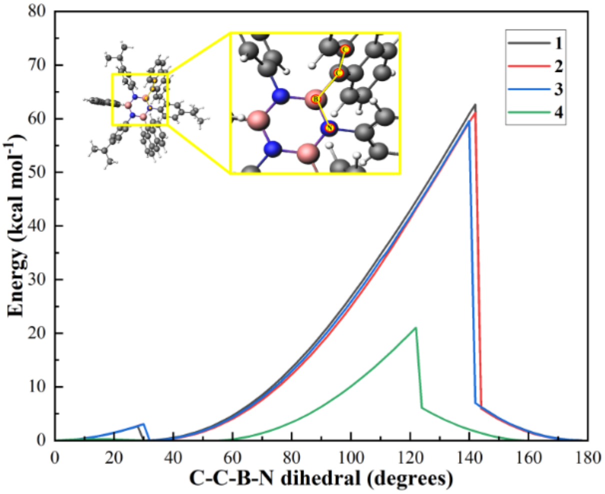

Figure S6.2 DFT energy scan (kcal mol^{-1}) along the same C-C-B-N dihedral angle (degrees) for borazine 1, 2, 3, and 4, in black, red, blue, and green lines, respectively. The yellow inset shows the representative C-C-B-N dihedral angle for all borazines.

6.5.2 Synthesis

Chemical reagents were purchased from commercial suppliers and used without further purification. Solvents were dried over 4 Å mol sieves and purged with Argon before use. Flash column chromatography was performed on silica gel 60 Å (0.04 – 0.063 mm, Screening Devices B.V.). Thin Layer Chromatography (TLC) was performed on TLC Silica gel 60 plates (Kieselgel F254, Merck). Liquid-state NMR spectra were recorded on a Bruker AV-400WB NMR instrument. Chemical shifts are given in ppm (δ) relative to the solvent signals ($CDCl_3$). Electrospray ionization mass spectra (ESI-MS) were obtained with a Thermo Scientific LCQ Fleet spectrometer equipped with an electrospray ion source (ESI) in positive ion mode. High-resolution mass spectra (HR-MS) were obtained with a Waters Synapt G2-Si (TOF) equipped with an ESI source in positive ion mode (source voltage 3.5 kV) and enkephalin (LeuEnk) as internal lock mass ($M+H^+$ = 556.2771). Elemental analysis was performed by Mikroanalytisches Labor Kolbe (c/o Fraunhofer Institut UMSICHT).

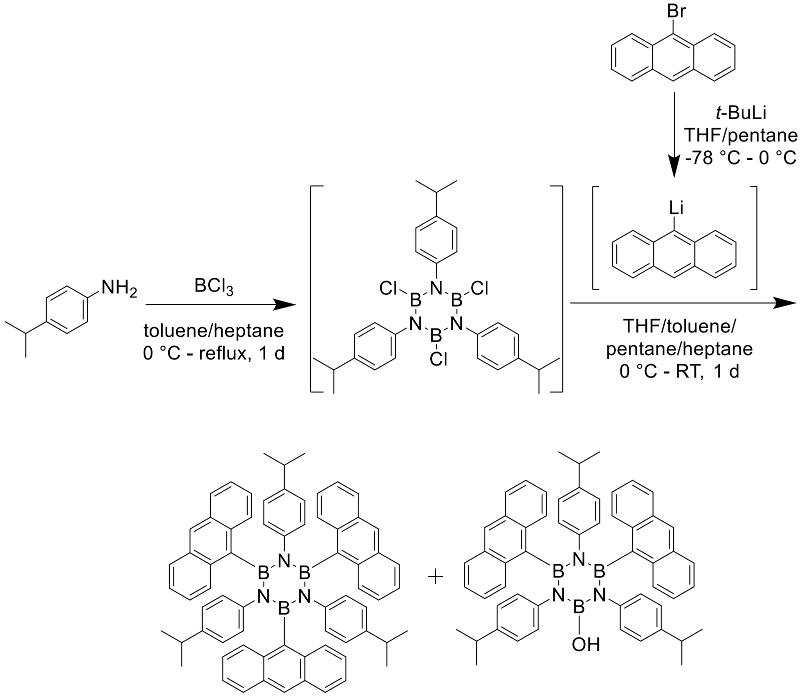

Borazine 2
17%

Borazine 5
28%

Scheme S6.1 Synthesis scheme of borazine 2 and 5.

B,B′,B′′-Tri(9-anthryl)-N,N′,N′′-tris(p-isopropyl-phenyl) borazine (2)

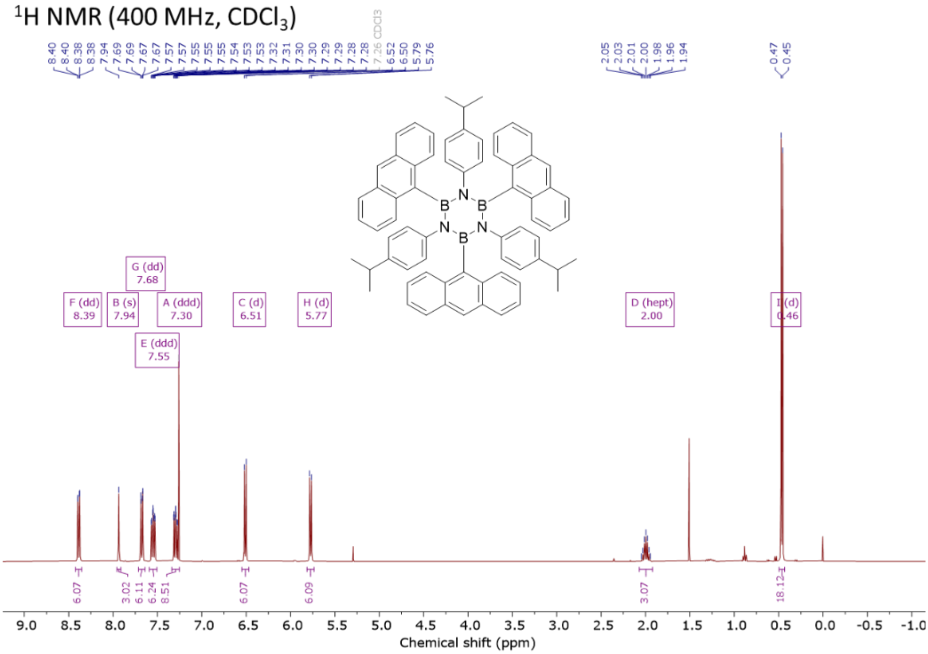

Figure S6.3 ^{1}H NMR spectrum of borazine 2 in CDCl$_3$.

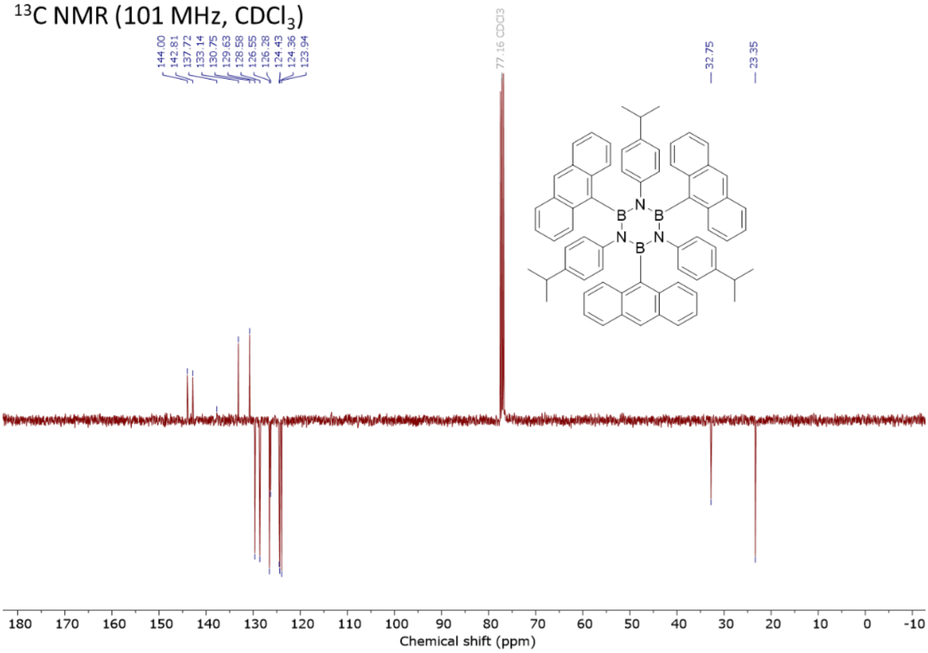

Figure S6.4 ^{13}C NMR spectrum of borazine 2 in CDCl$_3$.

B,B′-Tri(9-anthryl)-B″-hydroxy-N,N′,N″-tris(p-isopropyl-phenyl) borazine (5)
Following the same experimental procedure as for borazine **2**, the bisanthryl-substituted borazine **5** was synthesized and purified (Rf = 0.5 in DCM/pentane 3:7) as yellow crystals (75 mg, 0.093 mmol, 28%). ^{1}H NMR (400 MHz, $CDCl_3$) δ 8.27 (dd, J = 8.7, 1.1 Hz, 4H), 7.93 (s, 2H), 7.67 (dd, J = 8.0, 1.2 Hz, 4H), 7.49 (ddd, J = 8.6, 6.6, 1.3 Hz, 4H), 7.29 (ddd, J = 8.4, 6.5, 1.1 Hz, 4H), 6.96 (d, J = 8.3 Hz, 4H), 6.62 (d, J = 8.3 Hz, 4H), 6.32 (d, J = 8.4 Hz, 2H), 5.66 (d, J = 8.4 Hz, 2H), 3.81 (s, 1H), 2.50 (heptet, J = 6.9 Hz, 2H), 1.93 (heptet, J = 6.8 Hz, 1H), 0.91 (d, J = 6.9 Hz, 12H), 0.41 (d, J = 6.9 Hz, 6H). ^{13}C NMR (101 MHz, $CDCl_3$) δ 145.4, 143.7, 142.7, 141.0, 137.4, 133.1, 130.7, 129.6, 128.5, 127.1, 126.6, 126.2, 126.1, 124.38, 124.35, 123.7, 33.2, 32.7, 23.7, 23.3. ESI MS m/z 803.4 (M^+). HR-MS m/z 804.4, 821.5 ($M+H^+$, $M+NH_4^+$). Anal. Calcd for $C_{55}H_{52}B_3N_3{\cdot}5H_2O$: C, 73.93; H, 6.99; N, 4.70. Found: C, 73.18; H, 6.61; N, 4.62.

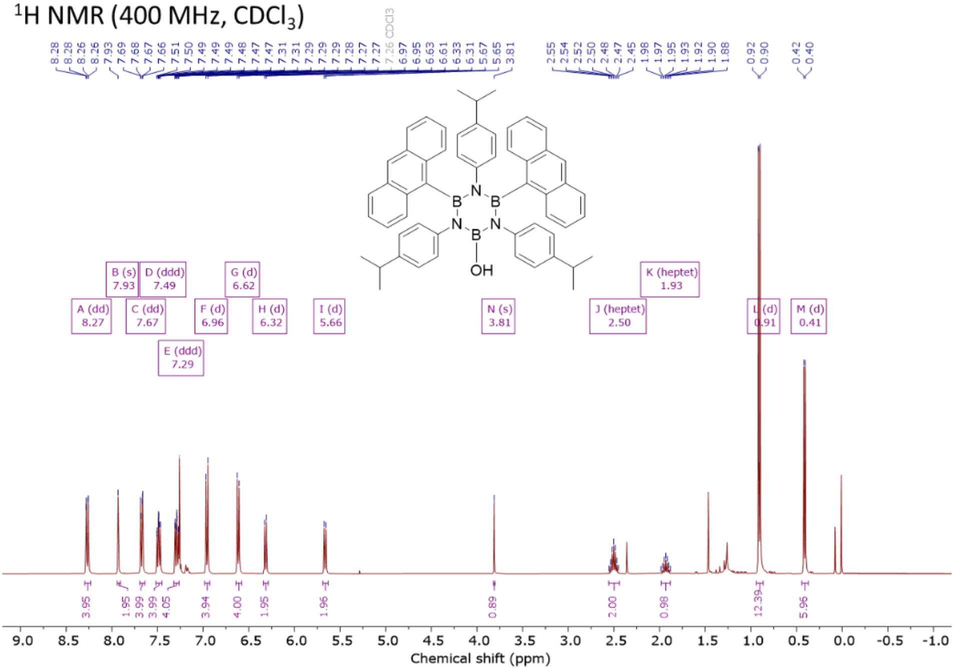

Figure S6.5 ^{1}**H NMR spectrum of borazine 5 in $CDCl_3$.**

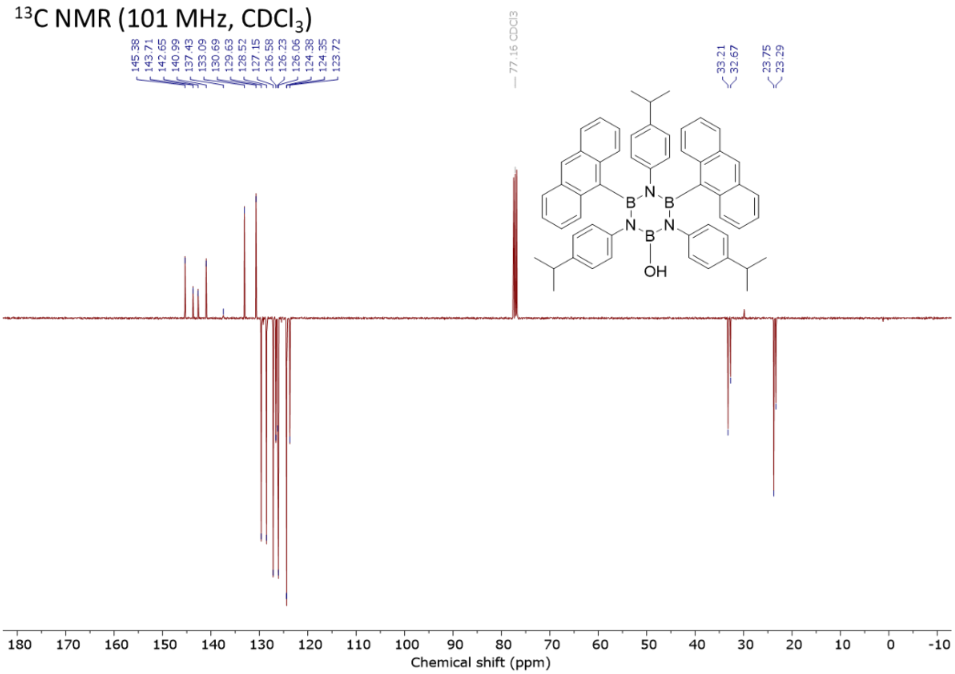

Figure S6.6 ^{13}**C NMR spectrum of borazine 5 in CDCl**$_3$**.**

6.5.3 Single Crystal X-ray Crystallography of [borazine 2 (toluene)]

2_203K: All reflection intensities were measured at 203(2) K* using a SuperNova diffractometer (equipped with Atlas detector) with Mo *K*α radiation (λ = 0.71073 Å) under the program CrysAlisPro (Version CrysAlisPro 1.171.42.49, Rigaku OD, 2022). The same program was used to refine the cell dimensions and for data reduction. The structure was solved with the program SHELXS-2018/3 (Sheldrick, 2018), and was refined on F^2 with SHELXL-2018/3 (Sheldrick, 2018).[68] Numerical absorption correction based on gaussian integration over a multifaceted crystal model was applied using CrysAlisPro. The temperature of the data collection was controlled using the system Cryojet (manufactured by Oxford Instruments). The H atoms were placed at calculated positions using the instructions AFIX 13, AFIX 33, AFIX 43 or AFIX 137 with isotropic displacement parameters having values 1.2 or 1.5 U_{eq} of the attached C atoms. The structure is partly disordered. Two of the three 4-isopropylphenyl groups and the lattice toluene solvent molecule are disordered over two orientations, and the occupancy factors of the major components of the disorder refine to 0.700(7), 0.53(2) and 0.502(8).

1_110K: All reflection intensities were measured at 110 K** using a SuperNova diffractometer (equipped with Atlas detector) with Cu *K*α radiation (λ = 1.54178 Å) under the program CrysAlisPro (Version CrysAlisPro 1.171.42.49, Rigaku OD, 2022). The same program was used to refine the cell dimensions and for data reduction. The structure was solved with the program SHELXS-2018/3 (Sheldrick, 2018) and was refined on F^2 with SHELXL-2018/3 (Sheldrick, 2018).[68] Analytical numeric absorption correction using a multifaceted crystal model was applied using CrysAlisPro. The temperature of the data collection was controlled using the system Cryojet (manufactured by Oxford Instruments). The H atoms were placed at calculated positions using the instructions AFIX 13, AFIX 33, AFIX 43 or AFIX 137 with isotropic displacement parameters having values 1.2 or 1.5 U_{eq} of the attached C atoms. The structure is mostly ordered. The lattice toluene solvent molecule is disordered over two orientations, and the occupancy factor of the major component of the disorder refines to 0.783(3). The reduced triclinic unit (a = 10.04 Å, b = 15.59 Å, c = 20.39 Å, α = 69.68°, β = 87.15°, γ = 83.53°) was transformed using the transformation matrix ***T*** = **(1 0 0 / 0 -1 0 / 0 1 -1)** to that the transformed unit cell of the low-temperature phase (**2_110K**) have comparable settings with that of the higher-temperature phase (**2_203K**).

* Any attempts to flash-cool the crystals from room temperature to 110 K and 150 K were unsuccessful as the crystals suffered from significant crystal damage (the crystals shattered very quickly, and diffraction was very poor), which is due to a solid-solid phase transition. When another crystal was flash-cooled from room temperature to 203 K, the crystal quality remained intact, and the diffraction pattern was consistent with that of a single crystal.

** The same crystal that was used for **2_203K** has been used here for **2_110K**. After a full data set was collected at 203 K, the crystal was allowed to be slowly cooled down from 203 to 110 K in 35-45 min. At 110 K, the crystal is clearly colorless (and yellow at 203K). Throughout the cooling process, the crystal slightly cracked but the long-range order of the crystal remained mostly intact as the crystal diffracted well at higher resolution.

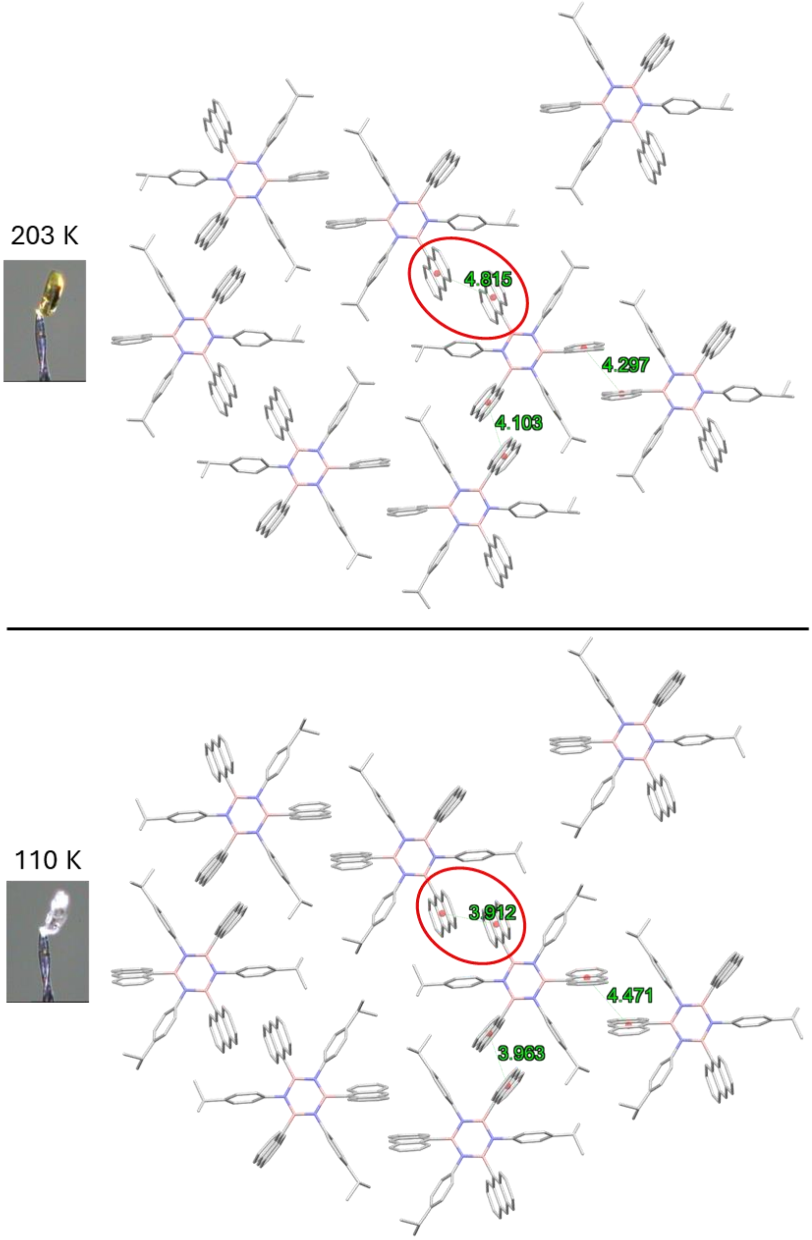

Figure S6.7 Crystal packing of the crystal structures of borazine 2 obtained from slow diffusion of pentane into a solution of borazine 2 in DCM:toluene 1:1 (v/v). Upon slow cooling from 203 K (top) to 110 K (bottom) the distance between anthracene moieties decreases from 4.815 to 3.912 Å (circled in red) along with a color change of the crystals from yellow to white.

Table S6.1 Crystallographic Data of 2_203K, CCDC 2409120 (https://www.ccdc.cam.ac.uk/structures/Search?access=referee&ccdc=2409120&Author=D.+Calvani)

	2_203K
Crystal data	
Chemical formula	$C_{69}H_{60}B_3N_3\cdot C_7H_8$
M_r	1055.76
Crystal system, space group	Triclinic, P-1
Temperature (K)	203
a, b, c (Å)	10.0141 (4), 15.7151 (9), 20.9899 (8)
□, □, □ (°)	110.870 (4), 91.583 (3), 96.480 (4)
V (Å^3)	3058.6 (3)
Z	2
Radiation type	Mo K□
□ (mm^{-1})	0.07
Crystal size (mm)	0.35 × 0.11 × 0.08
Data collection	
Diffractometer	SuperNova, Dual, Cu at zero, Atlas
Absorption correction	Gaussian *CrysAlis PRO* 1.171.42.49 (Rigaku Oxford Diffraction, 2022) Numerical absorption correction based on gaussian integration over a multifaceted crystal model Empirical absorption correction using spherical harmonics, implemented in SCALE3 ABSPACK scaling algorithm.
T_{min}, T_{max}	0.658, 1.000
No. of measured, independent and observed [I > 2□(I)] reflections	45752, 10743, 6934
R_{int}	0.060
(sin □/□)$_{max}$ (Å^{-1})	0.595
Refinement	
R[F^2 > 2□(F^2)], wR(F^2), S	0.062, 0.182, 1.04
No. of reflections	10743
No. of parameters	896
No. of restraints	871
H-atom treatment	H-atom parameters constrained
□ρ$_{max}$, □ρ$_{min}$ (e Å^{-3})	0.31, -0.28

Computer programs: *CrysAlis PRO* 1.171.42.49 (Rigaku OD, 2022), *SHELXS2018*/3 (Sheldrick, 2018), *SHELXL2018*/3 (Sheldrick, 2018), *SHELXTL* v6.10 (Sheldrick, 2008).[68]

Table S6.2 Crystallographic Data of 1_110K, CCDC 2409119 (https://www.ccdc.cam.ac.uk/structures/Search?access=referee&ccdc=2409119&Author=D.+Calvani)

	1_110K
Crystal data	
Chemical formula	$C_{69}H_{60}B_3N_3{\cdot}C_7H_8$
M_r	1055.76
Crystal system, space group	Triclinic, *P*-1
Temperature (K)	110
a, *b*, *c* (Å)	10.03783 (18), 15.5912 (3), 20.9249 (4)
α, β, γ (°)	113.9996 (18), 87.9640 (15), 96.4719 (15)
V (Å^3)	2972.42 (10)
Z	2
Radiation type	Cu *K*α
μ (mm^{-1})	0.51
Crystal size (mm)	0.35 × 0.11 × 0.08
Data collection	
Diffractometer	SuperNova, Dual, Cu at zero, Atlas
Absorption correction	Analytical *CrysAlis PRO* 1.171.42.49 (Rigaku Oxford Diffraction, 2022) Analytical numeric absorption correction using a multifaceted crystal model based on expressions derived by R.C. Clark & J.S. Reid. (Clark, R. C. & Reid, J. S. (1995). Acta Cryst. A51, 887-897) Empirical absorption correction using spherical harmonics, implemented in SCALE3 ABSPACK scaling algorithm.
T_{min}, T_{max}	0.866, 0.967
No. of measured, independent and observed [$I > 2\sigma(I)$] reflections	43342, 11627, 10034
R_{int}	0.029
$(\sin \theta/\lambda)_{max}$ (Å^{-1})	0.617
Refinement	
$R[F^2 > 2\sigma(F^2)]$, $wR(F^2)$, S	0.045, 0.131, 1.02
No. of reflections	11627
No. of parameters	804
No. of restraints	257
H-atom treatment	H-atom parameters constrained
$\Delta\rho_{max}$, $\Delta\rho_{min}$ (e Å^{-3})	0.49, -0.43

Computer programs: *CrysAlis PRO* 1.171.42.49 (Rigaku OD, 2022), *SHELXS2018*/3 (Sheldrick, 2018), *SHELXL2018*/3 (Sheldrick, 2018), *SHELXTL* v6.10 (Sheldrick, 2008).[68]

6.5.4 Comparison of experimental liquid-state NMR, solid-state NMR, and computational NMR spectra of carbon atoms in borazine 2

Liquid-state NMR spectra were recorded on Bruker Avance-III-HD 850 MHz standard bore NMR spectrometer. Solid-state NMR (SS-NMR) spectra were recorded on a Bruker Neo console 750 MHz wide bore spectrometer. Chemical shifts are given in ppm (δ) relative to their respective residual solvent signals (CD_2Cl_2).

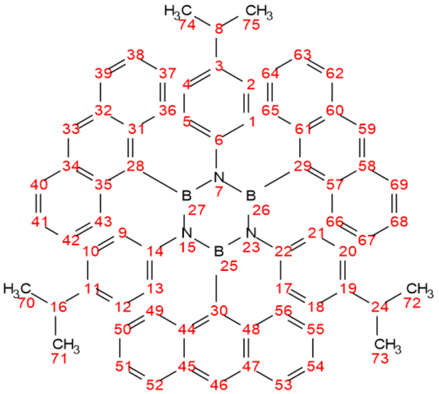

Figure S6.8 Structure of borazine 2 with labeled atom numbers for NMR assignment.

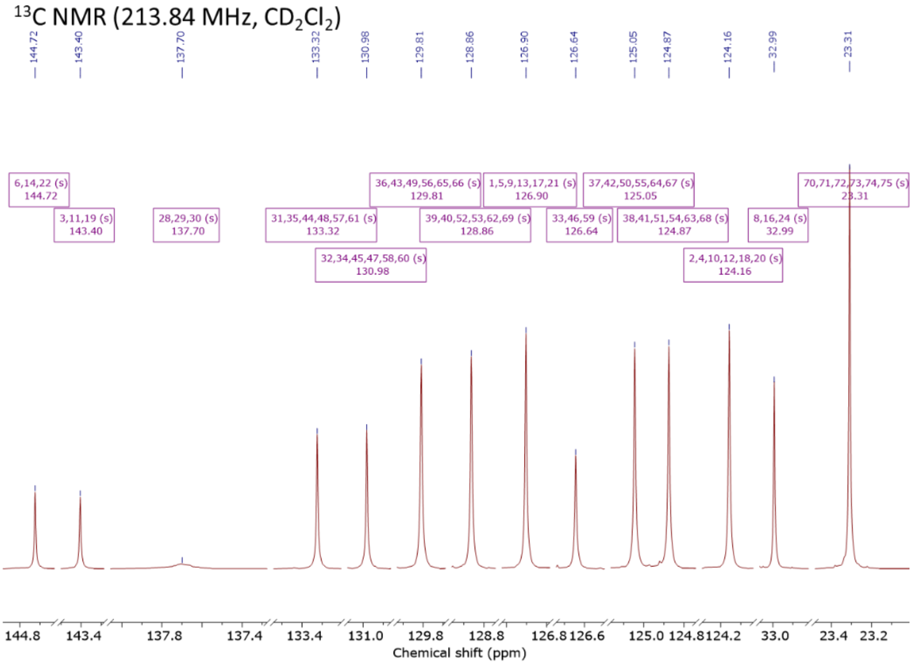

Figure S6.9 ^{13}C NMR spectrum of borazine 2 in CD_2Cl_2.

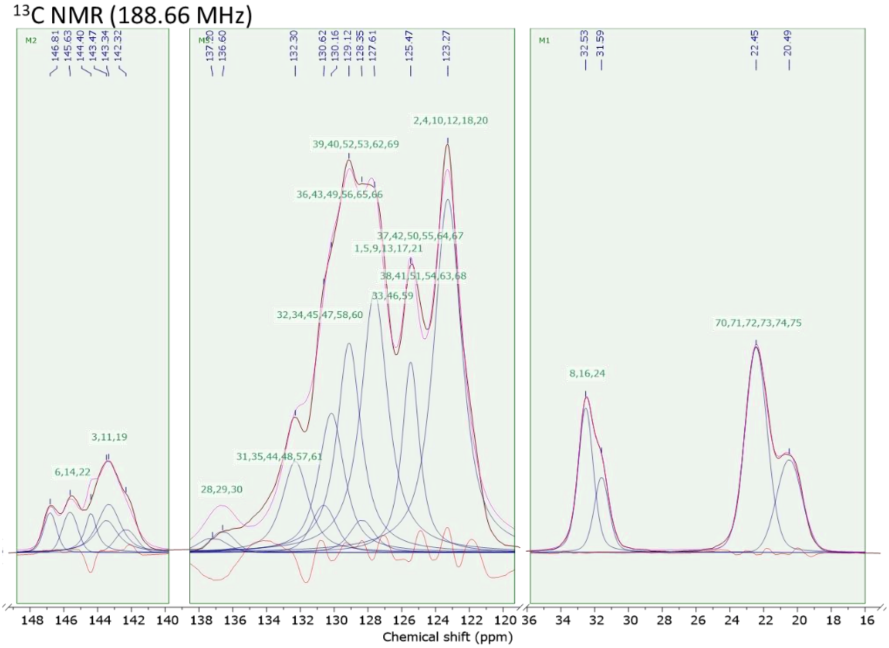

Figure S6.10 SS-NMR ^{13}C spectrum of the borazine 2 at 298 K.

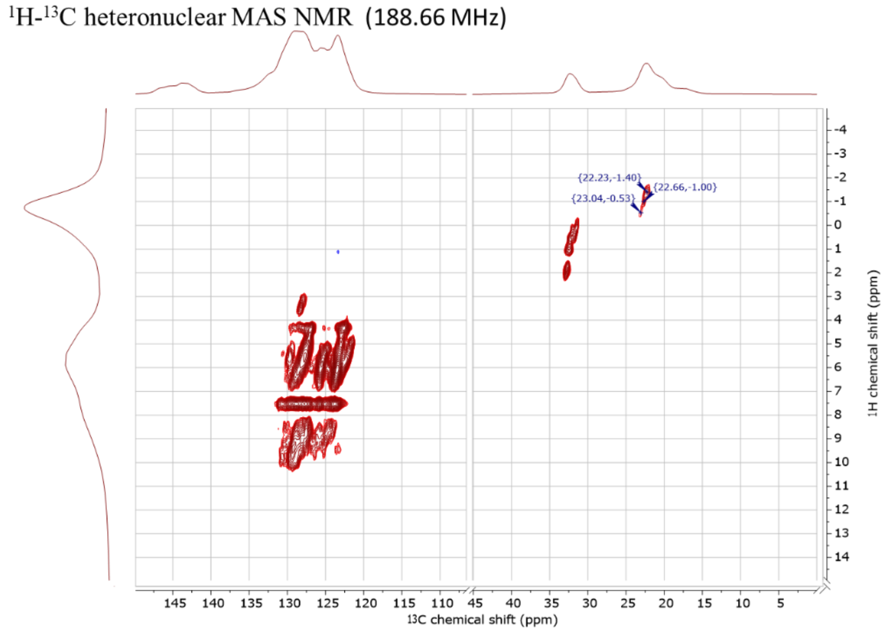

Figure S6.11 Contour plot sections of ^{1}H-^{13}C heteronuclear MAS NMR dipolar correlation spectra of borazine 2 recorded at a field of 17.6 T, employing a spinning rate of 20 kHz and sample temperatures of 298 K. The assignments of the CH_2 and CH_3 isopropyl signals are indicated.

Table S6.3 List of chemical shift values (in ppm) and assignments for carbon atoms in borazine 2 in liquid-state NMR (in CD_2Cl_2), solid-state NMR, and DFT (PBE-D3/TZP basis set) results for the monomer and dimer.

Signal number	Carbon atom number [a]	NMR in CD_2Cl_2 chemical shifts (ppm)	Solid-state NMR chemical shifts (ppm)	DFT monomer chemical shifts (ppm) [b]	DFT dimer chemical shifts (ppm) [c]
1	3	144.72	146.81	148.75	146.55
	11	144.72	145.63	146.70	145.61
	19	144.72	144.40	148.64	145.29
2	6	143.40	143.34	144.48	145.15
	14	143.40	142.32	144.71	144.80
	22	143.40	143.47	144.64	143.48
3	28	137.70	137.20	139.31	138.08
	29	137.70	136.60	139.31	139.22
	30	137.70	136.01	139.46	137.66
4	31,35,44,48,57,61	133.32	132.30	131.63	131.48
5	32,34,45,47,58,60	130.98	130.62	129.48	128.60
6	36,43,49,56,65,66	129.81	130.16	130.00	129.34
7	39,40,52,53,62,69	128.86	129.12	127.95	129.39
8	1,5,9,13,17,21	126.90	128.35	127.32	126.50
9	33,46,59	126.64	127.61	125.49	126.17
10	37,42,50,55,64,67	125.05	125.47	123.13	123.08
11	38,41,51,54,63,68	124.87	125.47	123.03	122.12
12	2,4,10,12,18,20	124.16	123.27	123.77	122.90
21	8	32.99	32.53	37.71	37.34
	16	32.99	31.59	45.01	36.34
	24	32.99	31.59	33.92	36.78
22	70,71,72	23.31	22.45	20.12	21.66
	73,74,75	23.31	20.49	17.77	20.42

[a] Numbering according to Figure S6.8

[b] STDEV = 2.44 ppm

[c] STDEV = 1.82 ppm

6.5.5 Langmuir-Blodgett film fabrication, Langmuir-Blodgett-like MD simulations, and surface-tension results

Spreading conditions at the water-to-air interface

A KSV NIMA mini trough (Biolin Scientific) with a surface area of 243 cm^2 equipped with a platinum Wilhelmy plate was used. The trough was made of Teflon® and the barriers of hydrophilic Delrin®. The subphase was Millipore water. For cleaning, the trough was first rinsed with Millipore water (3x), then wiped with chloroform:methanol 3:1 (v:v) with dust-free paper, and finally rinsed with Millipore water again. The barriers were wiped with Millipore water and chloroform with dust-free paper. The trough was then filled with Millipore water, and the surface was cleaned by aspiration to remove any residual particles. For spreading experiments, analytical grade chloroform (>99,9%, stabilized with amylene) was freshly distilled using clean glassware, stored in the dark, and used within 2 weeks. Distillation has a small effect on removing chloroform contamination at larger volumes, as the isotherm is shifted to higher MMAs at larger volumes (Figure S6.12). However, no significant differences in thin film properties were found from AFM and SEM analyses. Stock solutions of borazine **2** or POPC in chloroform were prepared at 1 mg mL^{-1} and then further diluted to the respective concentrations. Spreading was performed using a 100 µL air-tight Hamilton syringe equipped with a Hamilton Kel-F hub blunt point (26s gauge) needle. The solution was carefully spread at the interface by bringing the droplets hanging from the syringe into contact with the water surface at a rate of ~20 µL min^{-1}. The stock solutions were stored in the dark at 4 °C and used within 2 weeks. The compression was started 20 min after spreading to allow complete evaporation of the solvent at a speed of 2 mm min^{-1}. After reaching the desired surface pressure, the Langmuir film was allowed to stabilize for 15 min before deposition onto a solid substrate. The average and standard deviation were calculated from two replicates (for 23 nmol in 44 µL) or four replicates (for 23 nmol in 110, 220, and 440 µL) in OriginPro 2002 using the Average Multiple Curve; average following curve trace; 1000 points; and linear interpolation.

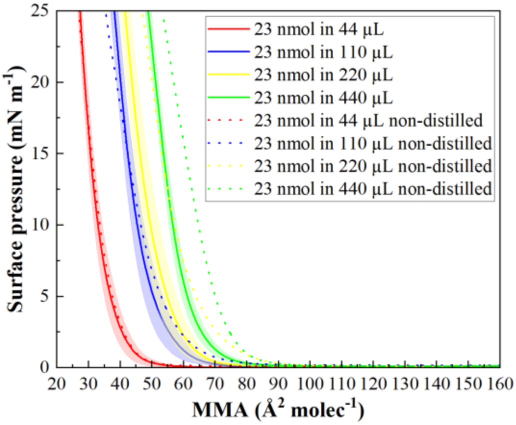

Figure S6.12 Effect of solvent distillation on the isotherms after depositing 23 nmol borazine 2 in increasing amounts of $CHCl_3$, where the surface pressure in mN m^{-1} depends on the mean molecular area (MMA) in $Å^2$ molec^{-1}. At lower volumes, the additional solvent distillation has no effect. However, at higher volumes, the isotherms are shifted to higher mean molecular area (MMA) values for non-distilled chloroform, indicating that at higher volumes, solvent contamination could play a role.

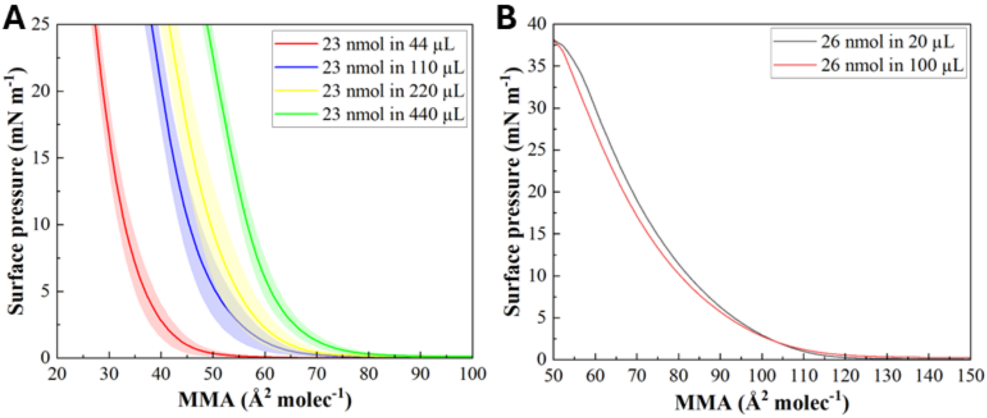

Figure S6.13 Langmuir-Blodgett isotherms of borazine 2 and POPC. (A) Isotherms of the borazine **2** system after depositing 23 nmol borazine **2** in increasing amounts of $CHCl_3$, where the surface pressure in mN m^{-1} depends on the mean molecular area (MMA) in $Å^2$ molec^{-1}. Upon dilution, the isotherm is shifted to higher MMA values. The intersection of the extrapolated violet dashed line indicates the MMA at which the morphology that corresponds to the point of tangency (in this case 2 mN m^{-1}) starts to take place if the film was perfectly distributed homogeneously. (B) Isotherm of 26 nmol POPC in increasing amounts of $CHCl_3$. Dilution does not affect the isotherm, indicating the ideal spreading behavior of POPC on the water surface during and after deposition.

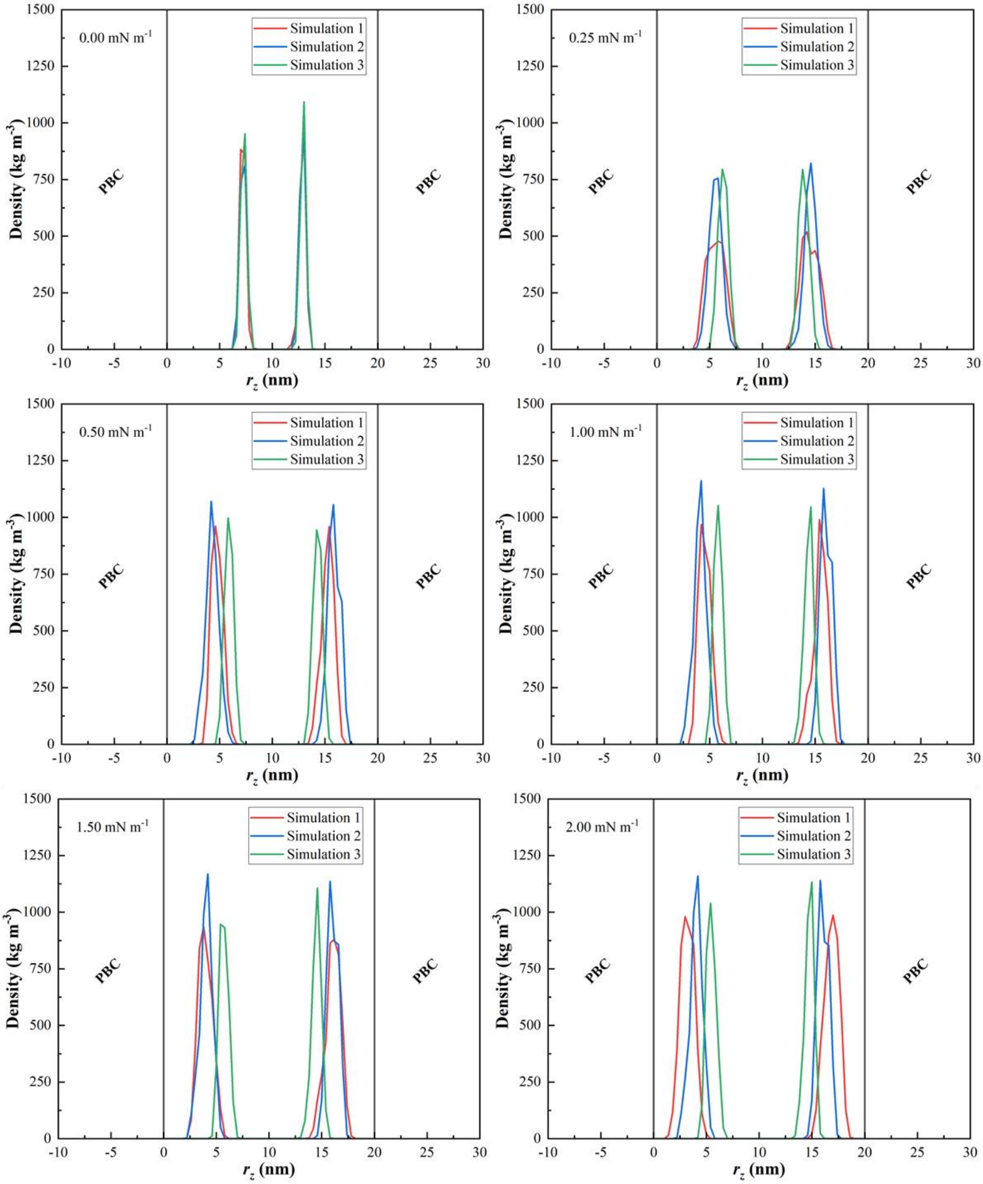

Figure S6.14 Density curve (kg m^{-3}) of the borazine 2 molecules along the *z*-coordinate r_z (nm) of the simulation box at different surface pressures (0, 0.25, 0.50, 1.00, 1.50, 2.00 mN m^{-1}) for the three independent MD simulations, in blue, red, and green solid lines, respectively. The edges of the simulation box along the *z*-coordinate are indicated with the vertical solid black lines, and the rest is repeated by the periodic boundary conditions (PBC).

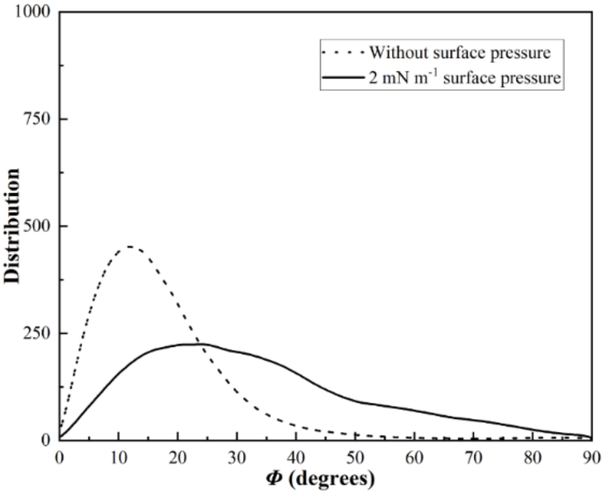

Figure S6.15 The distribution of the tilt angle (*Φ*) of the borazines 2 before compression at 300 K (without surface pressure - black dashed line), and after compression at 300 K (2 mN m^{-1} surface pressure – black solid line), extracted from the average over the 3 separate MD simulations for both cases. Distribution curves were obtained *via* Gaussian broadening with default standard deviation and normalized per amount of borazine molecules, using a kernel density estimation to produce this plot.

Transfer of Langmuir films onto substrates

Langmuir films were transferred onto silicon and quartz substrates *via* the Langmuir-Blodgett method. Si/SiO$_2$ wafers were purchased from Siegert Wafer (part-no. Z14102). Quartz slides were purchased from Alfa Aesar (prod. no. 42297). These substrates were cleaned by sonicating in demi water, acetone, ethanol, and isopropanol for 10 minutes sequentially, then rinsed with isopropanol and dried with pressurized nitrogen. Before deposition, the substrates were treated with oxygen plasma for 3 min and used within a day. For uniform thin films on Si/SiO$_2$, a slight contrast was visible on the optical microscope (Figure S6.16). Langmuir films were transferred onto silicon and quartz substrates *via* the Langmuir-Blodgett technique at a constant deposition speed of 0.5 mm min^{-1} unless specified otherwise, and dried over air. Langmuir films were transferred onto copper/QUANTIFOIL TEM grids *via* the Langmuir-Schaefer method, and dried over air. R0.6/1 QUANTIFOIL on copper 200 mesh TEM grids were purchased from Van Loenen instruments (S180-1) and used without further manipulation. Glow discharging the grids was found to negatively impact the success rate of freestanding film formation.

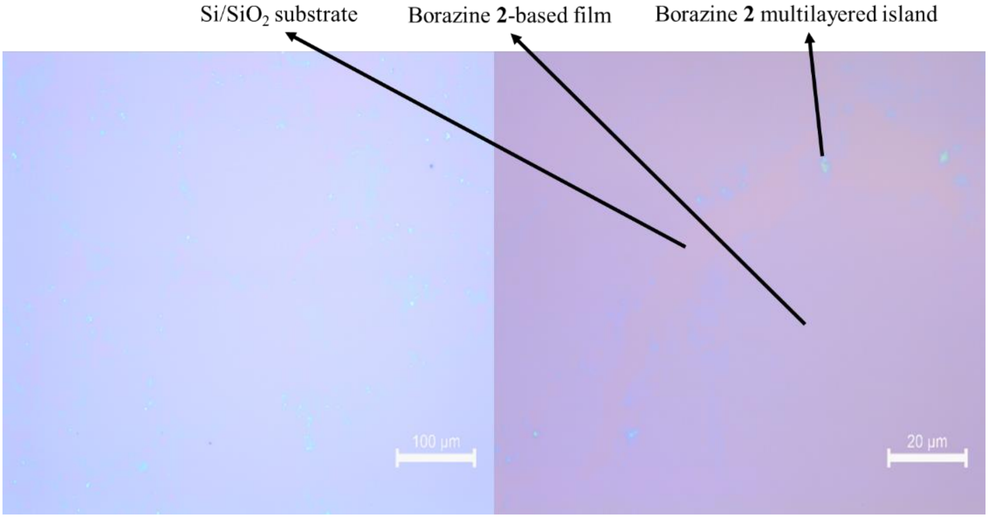

Figure S6.16 Optical images of the Langmuir-Blodgett film at 20× (left) and 100× (right) magnifications. Due to the low contrast between substrate and film, we added black arrows indicating the borazine **2**-based film, the borazine **2** multilayered island, and the Si/SiO_2 substrate.

6.5.6 Langmuir-Blodgett film thickness analysis and freestanding ability *via* SEM, AFM, and spectroscopy

SEM images were measured on an Apreo SEM (Thermo Fisher Scientific) instrument. Typical conditions were a T2 detector with the Optiplan Use case, an acceleration voltage of 2 kV, and a beam current of 13-100 pA. Images were captured at a resolution of 1536 × 1060, dwell times of 0.2 µs, 10 integrations, and relatively high contrast and brightness levels. At lower contrast and brightness levels, the films were not visible. TEM experiments were conducted on an image-side Cs-corrected FEI Titan 80-300 microscope operated at 300 kV. AFM was measured on a JPK Nanowizard 4 Ultra Speed AFM (Bruker Nano GmbH) instrument in tapping mode. Samples on Si/SiO_2 were measured using a 160AC-NA probe from OPUS with a resonant frequency of 300 kHz and a spring constant of 26 mN m^{-1}. Samples on Cu/QUANTIFOIL TEM grids were measured using an OMCL-AC240TS probe from OLYMPUS with a resonant frequency of 70 kHz and a spring constant of 2 mN m^{-1}. Typically, the images were captured at a resolution of 1024 × 1024 with a line scan rate of 1 Hz. AFM images were further processed using JPK Data Processing Software. UV-Vis spectroscopy was performed on a Cary 60 (Agilent) instrument. Fluorescence spectroscopy was performed on an FLS900 fluorescence (Edinburgh Instruments Ltd.) spectrometer equipped with a 450 W Xenon lamp.

Solutions were measured in a quartz cuvette cell with a path length of 1 cm. Langmuir-Blodgett films and spin-coated layers were measured on a quartz slide.

Langmuir-Schaefer films were found to be unstable upon measurement with the SEM (Figure S6.17B). No crystallinity could be detected from selective area electron diffraction (SAED) with the TEM (Figure S6.17C). Moreover, freestanding films could not be obtained when transferring onto QUANTIFOIL containing 2 µm holes.

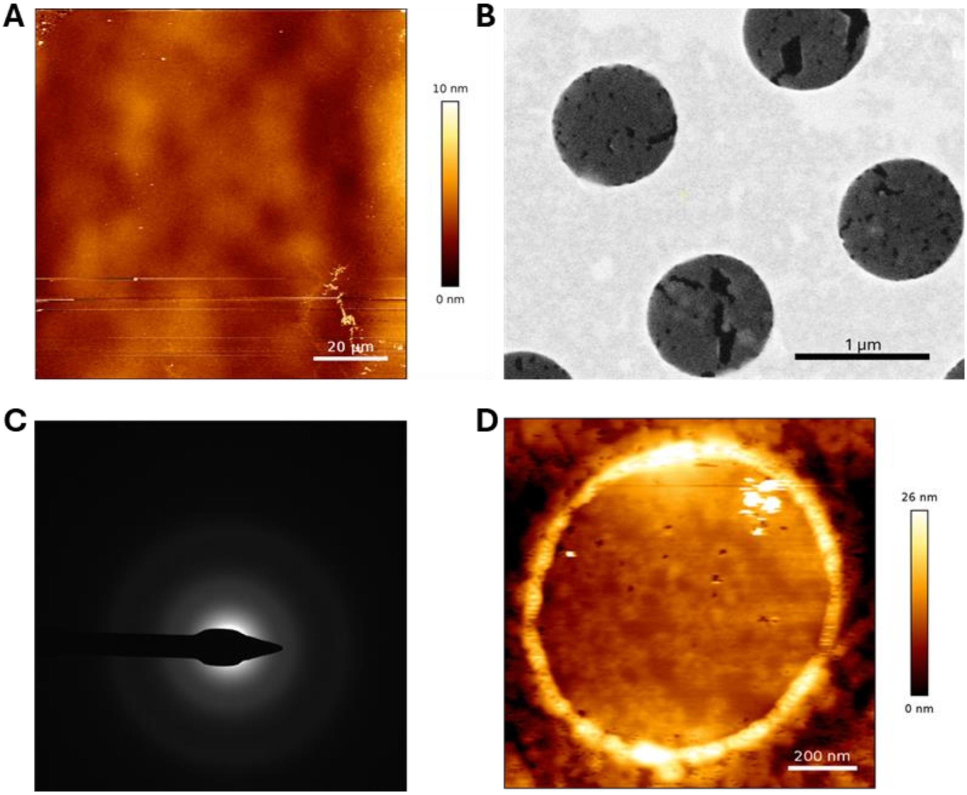

Figure S6.17 Homogeneity and freestanding ability of the borazine 2 thin films after transfer. (A) AFM images of a borazine Langmuir-Blodgett film prepared from 0.05 mg mL^{-1} in $CHCl_3$ transferred on Si/SiO_2 at a constant surface pressure of 2 mN m^{-1}: uniform flake spanning an area of 100 × 100 µm. (B) SEM images at 50000× magnification (blue scale bar, 1 µm) of Langmuir-Schaefer films prepared from 0.05 mg mL^{-1}, compressed to 2 mN m^{-1}, on QUANTIFOIL grid perforated with an array of 0.6 µm diameter holes on a copper TEM grid. The films covering the holes were found to collapse upon prolonged electron beam irradiation. (C) No crystallinity could be detected from SAED. (D) High magnification of AFM analysis of Figure 6.5D of Langmuir-Schaefer films obtained from 0.05 mg mL^{-1}, compressed to 2 mN m^{-1}, on QUANTIFOIL containing 0.6 µm holes on a copper TEM grid before the SEM.

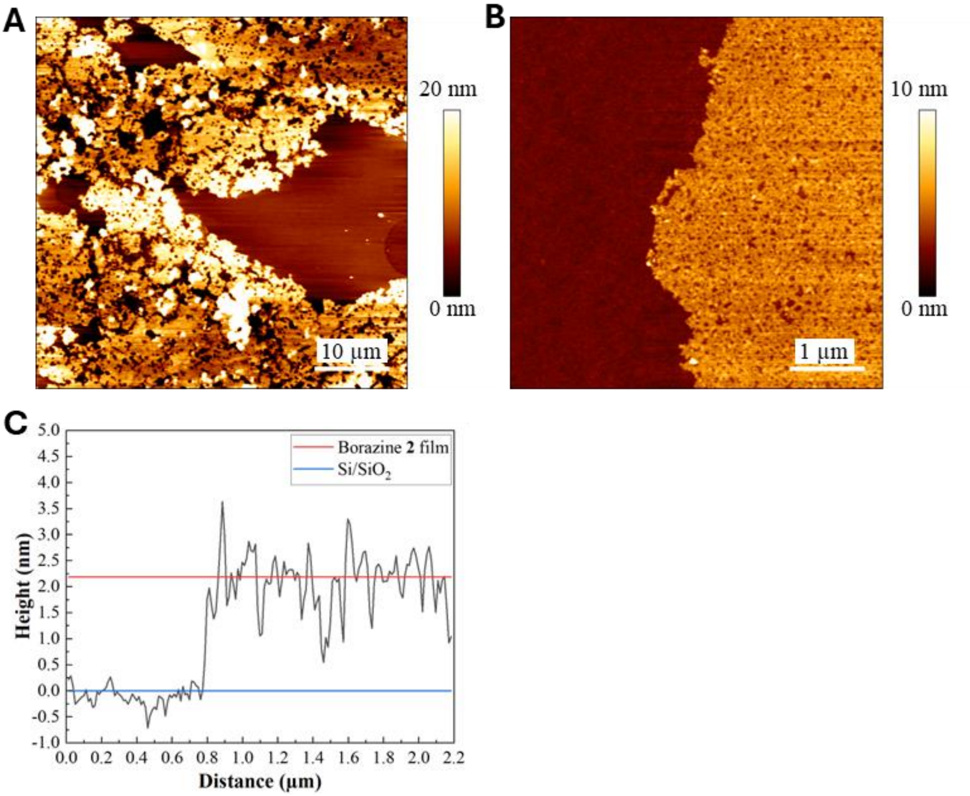

Figure S6.18 AFM images of borazine 2 films prepared from 0.05 mg mL^{-1} in $CHCl_3$ transferred on Si/SiO_2 at a constant surface pressure of 15 mN m^{-1}. (A) High degree of aggregation was found in these films between some uniform flakes at a magnification to 50 × 50 µm. (B) A magnification to 5 × 5 µm on a crack in the film, where the cross-section (C) was plotted resulting in an estimated height of 2.2 nm.

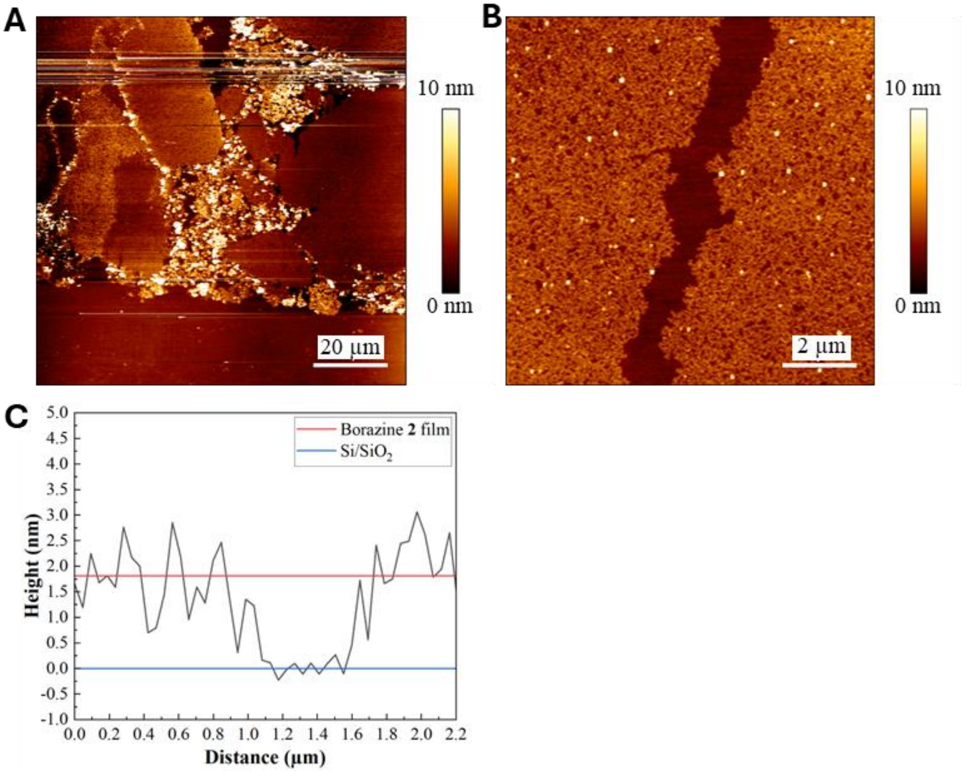

Figure S6.19 AFM images of borazine films prepared from 0.2 mg mL^{-1} in CHCl$_3$ transferred onto Si/SiO$_2$ at a constant surface pressure of 2 mN m^{-1}. (A) High frequency of large particles and clusters was found in these films at a magnification to 100 × 100 µm. (B) A magnification to 10 × 10 µm on a crack in the film, where the cross-section (C) was plotted resulting in an estimated height of 1.8 nm.

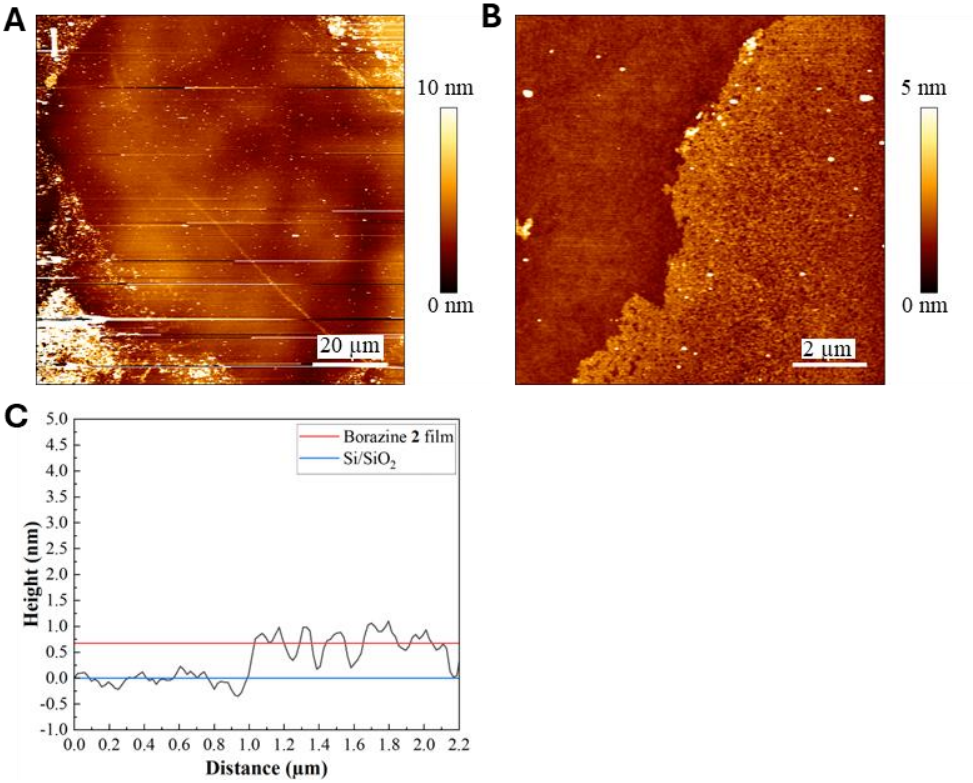

Figure S6.20 AFM images of borazine films prepared from 0.2 mg mL^{-1} in CHCl$_3$ transferred at a constant surface pressure of 2 mN m^{-1} and fast transport rate onto the Si/SiO$_2$ substrate of 2.5 mm min^{-1}. (A) High frequency of large particles and clusters was found in these films at a magnification to 100 × 100 µm. (B) A magnification to 10 × 10 µm on a crack in the film, where the cross-section (C) was plotted resulting in an estimated height of 0.7 nm corresponding to a borazine **2**-based monolayer film.

6.5.7 Fluorescence Spectroscopy and TD-DFT Calculations

To shed light on the electronic structure and optical properties of the borazine **2**, time-dependent density functional theory (TD-DFT) calculations in PCM solvation were carried out (see Computational Methods in the main text). Starting from the harmonic vibrational spectra of the ground and excited states, the vibrationally resolved spectra were computed using the FCclasses3 program[34] and compared with experimental values (Figure 6.6, and Figure S6.21). The agreement between the computed and experimental absorption and fluorescence spectra is excellent for the borazine **2** monomer (Figure 6.6, and Figure S6.21). The computational fluorescence spectra show the characteristic features of the anthracene functionalization in borazine **2** with major peaks in the range between 420-460 nm, confirming the experimental values.[5] These results align with the optoelectronic characteristics observed in similar anthracene-based aggregates, hinting at intriguing potential applications in (opto)electronic devices.[5,7,16]

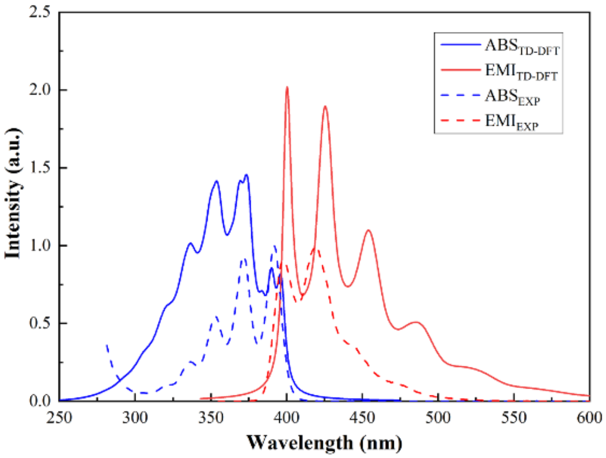

Figure S6.21 Computational (solid line) and experimental (dashed line) absorption (ABS in blue) and fluorescence (EMI in red) spectra, with intensity in atomic units (a.u.) and wavelength in nm. The computational spectra are calculated at the TD-DFT level with CAM-B3LYP functional and with Polarizable Continuum Model (PCM) $CHCl_3$ solvation.

6.5.8 Computational Methods

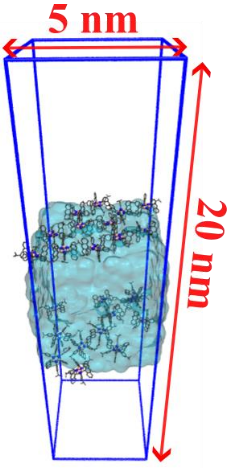

Figure S6.22 Schematic representation of the simulation box (5.0 × 5.0 × 20.0 nm^3) used for all the simulations with borazine 2 represented by balls and sticks. Boron, carbon, nitrogen, and fluorine are colored in pink, grey, blue, and cyan, respectively, hydrogens are omitted for clarity, and the water bulk shown with a light-blue surface.

6.6 References

(1) Bonifazi, D.; Fasano, F.; Lorenzo-Garcia, M. M.; et al. Boron-Nitrogen Doped Carbon Scaffolding: Organic Chemistry, Self-Assembly and Materials Applications of Borazine and Its Derivatives. *Chem. Commun.* **2015**, *51* (83), 15222–15236. https://doi.org/10.1039/c5cc06611e.

(2) Marchionni, D.; Basak, S.; Khodadadi, A. N.; et al. Synthesis and Applications of Organic Borazine Materials. *Adv. Funct. Mater.* **2023**, *33* (49), 2303635. https://doi.org/10.1002/adfm.202303635.

(3) Macha, M.; Marion, S.; Nandigana, V. V. R.; et al. 2D Materials as an Emerging Platform for Nanopore-Based Power Generation. *Nat. Rev. Mater.* **2019**, *4* (9), 588–605. https://doi.org/10.1038/s41578-019-0126-z.

(4) Mogg, L.; Zhang, S.; Hao, G.-P.; et al. Perfect Proton Selectivity in Ion Transport through Two-Dimensional Crystals. *Nat. Commun.* **2019**, *10* (1), 4243. https://doi.org/10.1038/s41467-019-12314-2.

(5) Wakamiya, A.; Ide, T.; Yamaguchi, S. Toward π-Conjugated Molecule Bundles: Synthesis of a Series of B,B′,B″-Trianthryl-N,N′,N″-Triarylborazines and the Bundle Effects on Their Properties. *J. Am. Chem. Soc.* **2005**, *127* (42), 14859–14866. https://doi.org/10.1021/ja0537171.

(6) Sham, I. H. T.; Kwok, C.-C.; Che, C.-M.; et al. Borazine Materials for Organic Optoelectronic Applications. *Chem. Commun.* **2005**, No. 28, 3547. https://doi.org/10.1039/b504510j.

(7) Kervyn, S.; Fenwick, O.; Di Stasio, F.; et al. Polymorphism, Fluorescence, and Optoelectronic Properties of a Borazine Derivative. *Chem. - Eur. J.* **2013**, *19* (24), 7771–7779. https://doi.org/10.1002/chem.201204598.

(8) Dosso, J.; Tasseroul, J.; Fasano, F.; et al. Synthesis and Optoelectronic Properties of Hexa-*peri*-hexabenzoborazinocoronene. *Angew. Chem. - Int. Ed.* **2017**, *56* (16), 4483–4487. https://doi.org/10.1002/anie.201700907.

(9) Wakchaure, V. C.; Lorenzo-García, M. M.; Fasano, F.; et al. Escape from Flatland: Stereoselective Synthesis of Hexa-aryl Borazines and Their sp^2-Based 3D Architectures. *Angew. Chem. Int. Ed.* **2024**, e202416700. https://doi.org/10.1002/anie.202416700.

(10) Kalashnyk, N.; Ganeshnagaswaran, P.; Kervyn, S.; et al. Self-Assembly of Decoupled Borazines on Metal Surfaces: The Role of the Peripheral Groups. *Chem. - Eur. J.* **2014**, *20* (37), 11856–11862. https://doi.org/10.1002/chem.201402839.

(11) Kervyn, S.; Kalashnyk, N.; Riello, M.; et al. “Magic” Surface Clustering of Borazines Driven by Repulsive Intermolecular Forces. *Angew. Chem. - Int. Ed.* **2013**, *52* (29), 7410–7414. https://doi.org/10.1002/anie.201300948.

(12) Sánchez-Sánchez, C.; Brüller, S.; Sachdev, H.; et al. On-Surface Synthesis of BN-Substituted Heteroaromatic Networks. *ACS Nano* **2015**, *9* (9), 9228–9235. https://doi.org/10.1021/acsnano.5b03895.

(13) Mohammed, M. S. G.; Colazzo, L.; Robles, R.; et al. Electronic Decoupling of Polyacenes from the Underlying Metal Substrate by sp^3 Carbon Atoms. *Commun. Phys.* **2020**, *3* (1), 159. https://doi.org/10.1038/s42005-020-00425-y.

(14) Liu, X.; He, M.; Calvani, D.; et al. Power Generation by Reverse Electrodialysis in a Single-Layer Nanoporous Membrane Made from Core–Rim Polycyclic Aromatic Hydrocarbons. *Nat. Nanotechnol.* **2020**, *15* (4), 307–312. https://doi.org/10.1038/s41565-020-0641-5.

(15) van der Ham, A.; Liu, X.; Calvani, D.; et al. Freestanding Non-Covalent Thin Films of the Propeller-Shaped Polycyclic Aromatic Hydrocarbon Decacyclene. *Nat. Commun.* **2022**, *13* (1), 4–11. https://doi.org/10.1038/s41467-022-29429-8.

(16) Servalli, M.; Celebi, K.; Payamyar, P.; et al. Photochemical Creation of Covalent Organic 2D Monolayer Objects in Defined Shapes *via* a Lithographic 2D Polymerization. *ACS Nano* **2018**, *12* (11), 11294–11306. https://doi.org/10.1021/acsnano.8b05964.

(17) Silva, N. J.; Machado, F. B. C.; Lischka, H.; et al. Π-Π Stacking Between Polyaromatic Hydrocarbon Sheets Beyond Dispersion Interactions. *Phys. Chem. Chem. Phys.* **2016**, *18* (32), 22300–22310. https://doi.org/10.1039/c6cp03749f.

(18) Dance, I. Inorganic Intermolecular Motifs, and Their Energies. *CrystEngComm* **2003**, *5* (37), 208. https://doi.org/10.1039/b304667m.

(19) Sinnokrot, M. O.; Sherrill, C. D. Substituent Effects in Π−π Interactions: Sandwich and T-Shaped Configurations. *J. Am. Chem. Soc.* **2004**, *126* (24), 7690–7697. https://doi.org/10.1021/ja049434a.

(20) Moussallem, C.; Allain, M.; Mallet, C.; et al. Fluorine–Fluorine Type II versus πF–π Stacking Interactions in the Supramolecular Organizations of Extended Thiophene Derivatives End Capped by Imino-Perfluorophenyl Units. *J. Fluor. Chem.* **2015**, *178*, 34–39. https://doi.org/10.1016/j.jfluchem.2015.06.018.

(21) Yi, H.; Albrecht, M.; Pan, F.; et al. Stacking of Sterically Congested Trifluoromethylated Aromatics in Their Crystals – The Role of Weak F···π or F···F Contacts. *Eur. J. Org. Chem.* **2020**, *2020* (38), 6073–6077. https://doi.org/10.1002/ejoc.202001008.

(22) Ganapathy, S.; Sengupta, S.; Wawrzyniak, P. K.; et al. Zinc Chlorins for Artificial Light-Harvesting Self-Assemble into Antiparallel Stacks Forming a Microcrystalline Solid-State Material. *Proc. Natl. Acad. Sci.* **2009**, *106* (28), 11472–11477. https://doi.org/10.1073/pnas.0811872106.

(23) Sear, R.; Chung, S.-W.; Markovich, G.; et al. Spontaneous Patterning of Quantum Dots at the Air-Water Interface. *Phys. Rev. E* **1999**, *59* (6), R6255–R6258. https://doi.org/10.1103/PhysRevE.59.R6255.

(24) Swierczewski, M.; Bürgi, T. Langmuir and Langmuir–Blodgett Films of Gold and Silver Nanoparticles. *Langmuir* **2023**, *39* (6), 2135–2151. https://doi.org/10.1021/acs.langmuir.2c02715.

(25) Huang, S.; Tsutsui, G.; Sakaue, H.; et al. Experimental Conditions for a Highly Ordered Monolayer of Gold Nanoparticles Fabricated by the Langmuir–Blodgett Method. *J. Vac. Sci. Technol. B Microelectron. Nanometer Struct. Process. Meas. Phenom.* **2001**, *19* (6), 2045–2049. https://doi.org/10.1116/1.1410943.

(26) Oliveira, O. N.; Caseli, L.; Ariga, K. The Past and the Future of Langmuir and Langmuir–Blodgett Films. *Chem. Rev.* **2022**, *122* (6), 6459–6513. https://doi.org/10.1021/acs.chemrev.1c00754.

(27) Hamley, I. W. Nanotechnology with Soft Materials. *Angew. Chem. Int. Ed.* **2003**, *42* (15), 1692–1712. https://doi.org/10.1002/anie.200200546.

(28) Kastler, M.; Pisula, W.; Wasserfallen, D.; et al. Influence of Alkyl Substituents on the Solution- and Surface-Organization of Hexa-*peri*-hexabenzocoronenes. *J. Am. Chem. Soc.* **2005**, *127* (12), 4286–4296. https://doi.org/10.1021/ja0430696.

(29) Sakamoto, J.; van Heijst, J.; Lukin, O.; et al. Two-Dimensional Polymers: Just a Dream of Synthetic Chemists? *Angew. Chem. Int. Ed.* **2009**, *48* (6), 1030–1069. https://doi.org/10.1002/anie.200801863.

(30) Hisamatsu, S.; Masu, H.; Takahashi, M.; et al. Pairwise Packing of Anthracene Fluorophore: Hydrogen-Bonding-Assisted Dimer Emission in Solid State. *Cryst. Growth Des.* **2015**, *15* (5), 2291–2302. https://doi.org/10.1021/acs.cgd.5b00081.

(31) Dai, Y.; Liu, H.; Geng, T.; et al. Pressure-Induced Excimer Formation and Fluorescence Enhancement of an Anthracene Derivative. *J. Mater. Chem. C* **2021**, *9* (3), 934–938. https://doi.org/10.1039/D0TC04677A.

(32) Hayashi, T.; Mataga, N.; Sakata, Y.; et al. Excimer Fluorescence and Photodimerization of Anthracenophanes and 1,2-Dianthrylethanes. *J. Am. Chem. Soc.* **1976**, *98* (19), 5910–5913. https://doi.org/10.1021/ja00435a027.

(33) Schillmöller, T.; Herbst-Irmer, R.; Stalke, D. Insights into Excimer Formation Factors from Detailed Structural and Photophysical Studies in the Solid-State. *Adv. Opt. Mater.* **2021**, *9* (8), 2001814. https://doi.org/10.1002/adom.202001814.

(34) Cerezo, J.; Santoro, F. *FCclasses3*: Vibrationally-resolved Spectra Simulated at the Edge of the Harmonic Approximation. *J. Comput. Chem.* **2023**, *44* (4), 626–643. https://doi.org/10.1002/jcc.27027.

(35) Adamo, C.; Barone, V. Toward Reliable Density Functional Methods without Adjustable Parameters: The PBE0 Model. *J. Chem. Phys.* **1999**, *110* (13), 6158–6170. https://doi.org/10.1063/1.478522.

(36) Ernzerhof, M.; Scuseria, G. E. Assessment of the Perdew–Burke–Ernzerhof Exchange-Correlation Functional. *J. Chem. Phys.* **1999**, *110* (11), 5029–5036. https://doi.org/10.1063/1.478401.

(37) Grimme, S.; Ehrlich, S.; Goerigk, L. Effect of the Damping Function in Dispersion Corrected Density Functional Theory. *J. Comput. Chem.* **2011**, *32* (7), 1456–1465. https://doi.org/10.1002/jcc.21759.

(38) Frisch, M. J.; Trucks, G. W.; Schlegel, H. B.; et al. Gaussian 16 Revision C. 01, 2016. *Gaussian Inc Wallingford CT* **2016**, *1*, 572.

(39) Perdew, J. P.; Burke, K.; Ernzerhof, M. Generalized Gradient Approximation Made Simple. *Phys. Rev. Lett.* **1996**, *77* (18), 3865–3868. https://doi.org/10.1103/PhysRevLett.77.3865.

(40) AMS 2023.1, SCM, Theoretical Chemistry, Vrije Universiteit, Amsterdam, The Netherlands. http://www.scm.com (accessed 2025-08-05).

(41) Berendsen, H. J. C.; van der Spoel, D.; van Drunen, R. GROMACS: A Message-Passing Parallel Molecular Dynamics Implementation. *Comput. Phys. Commun.* **1995**, *91* (1–3), 43–56. https://doi.org/10.1016/0010-4655(95)00042-E.

(42) Lindahl, E.; Hess, B.; van der Spoel, D. GROMACS 3.0: A Package for Molecular Simulation and Trajectory Analysis. *J. Mol. Model.* **2001**, *7* (8), 306–317. https://doi.org/10.1007/S008940100045.

(43) van der Spoel, D.; Lindahl, E.; Hess, B.; et al. GROMACS: Fast, Flexible, and Free. *J. Comput. Chem.* **2005**, *26* (16), 1701–1718. https://doi.org/10.1002/jcc.20291.

(44) Hess, B.; Kutzner, C.; van der Spoel, D.; et al. GROMACS 4: Algorithms for Highly Efficient, Load-Balanced, and Scalable Molecular Simulation. *J. Chem. Theory Comput.* **2008**, *4* (3), 435–447. https://doi.org/10.1021/ct700301q.

(45) Pronk, S.; Páll, S.; Schulz, R.; et al. GROMACS 4.5: A High-Throughput and Highly Parallel Open Source Molecular Simulation Toolkit. *Bioinformatics* **2013**, *29* (7), 845–854. https://doi.org/10.1093/bioinformatics/btt055.

(46) Abraham, M. J.; Murtola, T.; Schulz, R.; et al. Gromacs: High Performance Molecular Simulations through Multi-Level Parallelism from Laptops to

Supercomputers. *SoftwareX* **2015**, *1–2*, 19–25. https://doi.org/10.1016/j.softx.2015.06.001.

(47) Páll, S.; Abraham, M. J.; Kutzner, C.; et al. Tackling Exascale Software Challenges in Molecular Dynamics Simulations with GROMACS. *Lect. Notes Comput. Sci. Subser. Lect. Notes Artif. Intell. Lect. Notes Bioinforma.* **2015**, *8759*, 3–27. https://doi.org/10.1007/978-3-319-15976-8_1.

(48) York, D. M.; Darden, T. A.; Pedersen, L. G. The Effect of Long-Range Electrostatic Interactions in Simulations of Macromolecular Crystals: A Comparison of the Ewald and Truncated List Methods. *J. Chem. Phys.* **1993**, *99* (10), 8345–8348. https://doi.org/10.1063/1.465608.

(49) Bussi, G.; Donadio, D.; Parrinello, M. Canonical Sampling through Velocity Rescaling. *J. Chem. Phys.* **2007**, *126* (1). https://doi.org/10.1063/1.2408420.

(50) Horn, H. W.; Swope, W. C.; Pitera, J. W.; et al. Development of an Improved Four-Site Water Model for Biomolecular Simulations: TIP4P-Ew. *J. Chem. Phys.* **2004**, *120* (20), 9665–9678. https://doi.org/10.1063/1.1683075.

(51) Harris, J. G. Liquid-Vapor Interfaces of Alkane Oligomers: Structure and Thermodynamics from Molecular Dynamics Simulations of Chemically Realistic Models. *J. Phys. Chem.* **1992**, *96* (12), 5077–5086. https://doi.org/10.1021/j100191a062.

(52) Vega, C.; De Miguel, E. Surface Tension of the Most Popular Models of Water by Using the Test-Area Simulation Method. *J. Chem. Phys.* **2007**, *126* (15). https://doi.org/10.1063/1.2715577.

(53) Chen, F.; Smith, P. E. Simulated Surface Tensions of Common Water Models. *J. Chem. Phys.* **2007**, *126* (22), 2005–2008. https://doi.org/10.1063/1.2745718.

(54) Jorgensen, W. L.; Maxwell, D. S.; Tirado-Rives, J. Development and Testing of the OPLS All-Atom Force Field on Conformational Energetics and Properties of Organic Liquids. *J. Am. Chem. Soc.* **1996**, *118* (45), 11225–11236. https://doi.org/10.1021/ja9621760.

(55) Kaminski, G. A.; Friesner, R. A.; Tirado-Rives, J.; et al. Evaluation and Reparametrization of the OPLS-AA Force Field for Proteins *via* Comparison with Accurate Quantum Chemical Calculations on Peptides. *J. Phys. Chem. B* **2001**, *105* (28), 6474–6487. https://doi.org/10.1021/jp003919d.

(56) Martin, M. G. Comparison of the AMBER, CHARMM, COMPASS, GROMOS, OPLS, TraPPE and UFF Force Fields for Prediction of Vapor-Liquid Coexistence Curves and Liquid Densities. *Fluid Phase Equilibria* **2006**, *248* (1), 50–55. https://doi.org/10.1016/j.fluid.2006.07.014.

(57) Dodda, L. S.; Cabeza de Vaca, I.; Tirado-Rives, J.; et al. LigParGen Web Server: An Automatic OPLS-AA Parameter Generator for Organic Ligands. *Nucleic Acids Res.* **2017**, *45* (W1), W331–W336. https://doi.org/10.1093/nar/gkx312.

(58) Yadav, A.; Dindorkar, S. S.; Ramisetti, S. B.; et al. Simultaneous Adsorption of Methylene Blue and Arsenic on Graphene, Boron Nitride and Boron Carbon Nitride Nanosheets: Insights from Molecular Simulations. *J. Water Process Eng.* **2022**, *46*, 102653. https://doi.org/10.1016/j.jwpe.2022.102653.

(59) Marenich, A. V.; Jerome, S. V.; Cramer, C. J.; et al. Charge Model 5: An Extension of Hirshfeld Population Analysis for the Accurate Description of Molecular Interactions in Gaseous and Condensed Phases. *J. Chem. Theory Comput.* **2012**, *8* (2), 527–541. https://doi.org/10.1021/ct200866d.

(60) Humphrey, W.; Dalke, A.; Schulten, K. VMD: Visual Molecular Dynamics. *J. Mol. Graph.* **1996**, *14*, 33–38.

(61) Martínez, L.; Andrade, R.; Birgin, E. G.; et al. PACKMOL: A Package for Building Initial Configurations for Molecular Dynamics Simulations. *J. Comput. Chem.* **2009**, *30* (13), 2157–2164. https://doi.org/10.1002/jcc.21224.

(62) Fine, R. A.; Millero, F. J. Compressibility of Water as a Function of Temperature and Pressure. *J. Chem. Phys.* **1973**, *59* (10), 5529–5536. https://doi.org/10.1063/1.1679903.

(63) Yanai, T.; Tew, D. P.; Handy, N. C. A New Hybrid Exchange–Correlation Functional Using the Coulomb-Attenuating Method (CAM-B3LYP). *Chem. Phys. Lett.* **2004**, *393* (1–3), 51–57. https://doi.org/10.1016/j.cplett.2004.06.011.

(64) Tomasi, J.; Mennucci, B.; Cammi, R. Quantum Mechanical Continuum Solvation Models. *Chem. Rev.* **2005**, *105* (8), 2999–3094. https://doi.org/10.1021/cr9904009.

(65) Franck, J.; Dymond, E. G. Elementary Processes of Photochemical Reactions. *Trans Faraday Soc.* **1926**, *21* (February), 536–542. https://doi.org/10.1039/TF9262100536.

(66) Condon, E. U. Nuclear Motions Associated with Electron Transitions in Diatomic Molecules. *Phys. Rev.* **1928**, *32* (6), 858–872. https://doi.org/10.1103/PhysRev.32.858.

(67) Avila Ferrer, F. J.; Santoro, F. Comparison of Vertical and Adiabatic Harmonic Approaches for the Calculation of the Vibrational Structure of Electronic Spectra. *Phys. Chem. Chem. Phys.* **2012**, *14* (39), 13549. https://doi.org/10.1039/c2cp41169e.

(68) Sheldrick, G. M. Crystal Structure Refinement with *SHELXL*. *Acta Crystallogr. Sect. C Struct. Chem.* **2015**, *71* (1), 3–8. https://doi.org/10.1107/S2053229614024218.